PHOTOPHYSICAL PROPERTIES OF PLASMONIC GOLD NANOSTRUCTURES AND SEMICONDUCTING LEAD-HALIDE PEROVSKITE QUANTUM DOTS

A Dissertation

by

HSU-CHENG (OSCAR) CHENG

Submitted to the Office of Graduate and Professional Studies of
Texas A&M University
in partial fulfillment of the requirements for the degree of

DOCTOR OF PHILOSOPHY

Chair of Committee,	Dong Hee Son
Co-Chair of Committee,	Matthew Sheldon
Committee Members,	Simon North
	Alexey Belyanin
Head of Department,	Simon North

May 2021

Major Subject: Chemistry

ABSTRACT

Nanomaterials offer a unique platform to study the effect of morphology, light polarization, as well as quantum confinement on their photophysical properties. In this dissertation, two classes of nanomaterials – plasmonic gold nanostructures and semiconducting lead-halide perovskite quantum dots and their photophysical properties were explored.

In the first part of this work, plasmonic gold nanostructures subjected to circularly polarized illumination will generate static magnetic field as well as circular drift current. The light-induced static magnetic field in gold nanoparticle was measured for the first time, using time-resolved pump-probe Faraday rotation spectroscopy. The magnetization dynamics was instantaneous and coherent to incident light, reflecting its orbital angular momentum origin. Moreover, the circular drift current generated only under elliptical and circular polarized illumination results in a fundamental modification of electrical conductivity and plasmon dephasing time. Raman thermometry and photothermal effect were used to probe this modulation in a gold nanodisks array, and a qualitative agreement with our prediction was demonstrated.

The second part of this work is focused on the photoluminescence properties of strongly quantum confined $CsPbBr_3$ quantum dots, and the effect of their size and environment temperature. In contrast to other conventional semiconductor nanocrystals, such as II-VI, the photoluminescence peak position of $CsPbBr_3$ quantum dot was redshifted as the temperature decreased. In addition, the photoluminescence linewidth showed a strong size- and temperature- dependence, which can be attributed to strong

coupling to both longitudinal optical phonon and vibrational mode of ligands on the surface of quantum dots.

ACKNOWLEDGEMENTS

I would like to thank my advisor Dr. Son and Dr. Sheldon for allowing me to join their group and do research. They are both brilliant scientists with bold scientific ideas and high demand in details. They gave me room to explore and supported me pretty much any resources I needed. Also, their emphasis on the presentation skill is extremely useful not only in graduate school but also in my future career. I feel lucky to have both of them to be my advisor and I am really grateful for their guidance and support.

I also appreciate two senior group members: Dr. Daniel Rossi and Dr. Yitong Dong. Daniel taught me everything about the ultrafast laser system, optical alignment, spectroscopy and instrument control. Yitong gave me guidance on nanocrystals surface treatment and low temperature PL measurement. Both Daniel and Yitong were a scientific role model to me and I learned a lot from them.

I also want to thank other members from Son group: Dr. David Parobek always answered my questions on nanocrystals and covered me up on group matters; Dr. Jin and Doyun helped me with single particle measurement; Tian and Xueting provided perovskite samples and took TEM image for me; Joe worked on ultrafast laser system with me; Boqin worked on Raman microscope with me, and good luck on continuing my project. And members from Sheldon group: Dr. ShengXiang (Joey) Wu worked on Raman project with me; Dr. Nicki Hogan gave me advice on Lumerical simulation; Maelani helped me with supercomputer and AFM measurement; Ray helped me with my seminar talk and perovskite related questions; Zach and Annika fabricated plasmonic nanostructure for me. I also appreciate staffs in the chemistry department: Sandy helped me with all the

administration related matters; Jennifer helped our group with orders; Soon-Mi helped me with award application. I also want to thank our collaborators, Dr. Alexey Akimov and his research group in the Department of Physics.

Life in graduate school was not easy, so I want to thank all my friends in College Station. You guys brought me joys and reminded me of the importance of work life balance. I also want to thank my girlfriend Lisa for her love and support.

Finally, I would like to thank my family. Without their support, financially or mentally, I would not be able to study aboard and pursued my Ph.D. There is nothing I can do to return.

During my five and half years of graduate school, full of blood and tear is probably too exaggerative, but there was a lot of pressure and anxiety. However, I will never forget the joy after taking a good spectrum, and the feeling of accomplishment after an overnight experiment. Getting a Ph.D. is a tough process, but I am glad that I really enjoyed it.

CONTRIBUTORS AND FUNDING SOURCES

Contributors

This work was supervised by a dissertation committee consisting of Professor Dong Hee Son, Professor Matthew Sheldon, and Professor Simon North of the Department of Chemistry, and Professor Alexey Belyanin of the Department of Physics.

The gold nanodisks array in Chapter III was fabricated by Dr. Nicki Hogan, Zachary Brawly and Annika Lee of the Department of Chemistry. $CsPbBr_3$ sample in Chapter IV was synthesize by Tian Qian, Xueting Tang and Joseph Puthenpurayil of the Department of Chemistry. The optical components used in Figure II.6 and Figure III.7 were created by Alexander Franzen (ComponentLibrary by Alexander Franzen is licensed under a Creative Commons Attribution-NonCommercial 3.0 Unported License)

All other work conducted for this dissertation was completed by the student independently.

Funding Sources

This work is funded by National Science Foundation (Grant No. CHE-1836538), Gordon and Betty Moore Foundation (Grant No. GBMF6882), Air Force Office of Scientific Research (Grant No. FA9550-16-1-0154), Institute for Basic Science (Grant No. IBS-R026-D1) and the Welch Foundation (Grant No. A-1886)

NOMENCLATURE

LSPR	Localized Surface Plasmon Resonance
MO	Magneto-optical
IFE	Inverse Faraday Effect
RHCP	Right-handed Circular Polarization
LHCP	Left-handed Circular Polarization
AC	Alternative Current
DC	Direct Current
OD	Optical Density
AuNP	Gold Nanoparticle
OKE	Optical Kerr Effect
PL	Photoluminescence
CW	Continuous Wave
FWHM	Full Width at Half Maximum
ND	Neutral Density
HWP	Half Waveplate
QWP	Quarter Waveplate
LHP	Lead-Halide Perovskites
NC	Nanocrystals
QY	Quantum Yield
QD	Quantum Dots
LO	Longitudinal Optical Phonon

ε	Permittivity
ω_p	Plasma Frequency
ω	Optical Frequency
γ_b	Bulk Damping Rate
N	Electron Density
$\langle N \rangle$	Time-Averaged Electron Density
ε_0	Vacuum Permittivity
m_e	Effective Electron Mass
$\Delta\theta$	Optical Rotation Angle
$\vec{B}_{app}$	Applied Magnetic Field
υ	Verdet Constant
L	Effective Path Length
$\vec{M}_{ind}$	Induced Magnetization
λ	Wavelength of Light
c	Speed of Light
I	Intensity
σ	Electrical Conductivity
$\hat{E}$	Amplitude of an Oscillating Electric Field
k	Wavevector
$\langle j \rangle$	Time-Averaged Current Density
j_M	Magnetization Current

δ	Polarization Angle Difference Between the Pump and Probe Beam
ϕ	Ellipticity angle
n	Refractive Index
T_l	Lattice Temperature
T_e	Electronic Temperature
α	Sub-population of Hot Carriers
$\tau_{dephase}$	Plasmon Dephasing Time
a_B	Bohr Radius
μ_B	Bohr magneton
$\chi^{(3)}_{xxyy}$, $\chi^{(3)}_{xyyx}$	Third-Order Susceptibility
B_{eff}	Effective Magnetic Field
$f(E,T_l)$	Fermi-Dirac Distribution
$L(E,\tau_{dephase})$	Lorentzian Distribution Function
S(E)	Spectral Line Shape Function
E_{peak}	PL Peak Energy
Γ	Full Width at Half Maximum of Spectral Line Shape
Γ_{inh}	Inhomogeneous Broadening
γ_{LO}	LO Phonon Coupling Strength
k_b	Boltzmann Constant
γ_{ac}	Acoustic Phonon Coupling Strength
N_{LO}	Number of LO Phonon Mode

TABLE OF CONTENTS

Page

LIST OF FIGURES

Page

CHAPTER I

INTRODUCTION AND LITERATURE REVIEW

1.1 Overview

Nanoscience has brought tremendous interest in both academia and industry and has been a heart of modern technology. Nanomaterials possess distinct properties from their bulk counterpart, and the tunability is provided by their geometry, chemical composition, and surrounding environment. Understanding the effect of these parameters and the methodology to control the desired properties is essential to future applications. Photophysical properties, describing the interaction between light and matters, is one of the most important properties and affect daily applications in a comprehensive manner. For instance, nanostructure fabrication (ex: chip manufacturing), photovoltaic (ex: solar cell, photodetector), solid-state lightening (ex: light emitting diode and laser), and photocatalysis (ex: water splitting for hydrogen production). This dissertation will focus on fundamental understanding of photophysical properties of two classes of nanomaterials – plasmonic gold nanostructures and semiconducting lead-halide perovskite nanocrystals.

Plasmonic nanostructures – consisting of noble metals like gold, silver and copper – have fascinating optical properties that are tightly connected to the dynamics of conduction electrons within the metals. These conduction electrons move collectively, termed plasmon, in response to external electric field. Under circularly polarized light excitation, in which the electric field rotates in the plane perpendicular to propagation axis, coherent circular current in gold nanostructures can be generated. This light-induced

circular current leads to several interesting phenomenon, such as pronounced light-induced magnetic field and modulation of photothermal effect. The detailed discussion of these phenomenon and their mechanism will be presented in this dissertation.

On the other hand, lead-halide perovskite nanocrystals have received tremendous attention over a decade due to its excellent luminescence properties and record-breaking photovoltaic efficiency. The uniqueness of the lead-halide perovskite is that its luminescence and transport properties can be easily modulated by their physical size and chemical composition. In addition, the solution processability and low temperature synthesis condition makes it a cost-effective material system. The second half of the dissertation will be focused on extremely small lead-halide perovskite nanocrystals, so-called quantum dots. In the regime of strong quantum confinement, the optical properties, such as light absorption and photoluminescence, is strongly affected by the size and the surface of nanocrystals. Detailed studying on the effect of size and temperature will be presented in the dissertation.

1.2 Introduction to Light Induced Magnetism in Plasmonic Nanostructures

1.2.1 Noble Metal Nanostructures and Localized Surface Plasmon Resonance

Research on noble metal nanostructures, such as gold, silver and copper, have been received tremendous attention over the past several decades. This vigorous research field involves researchers from different expertise, including materials scientists designing novel nanostructures and optical properties, analytical chemists interested in single molecule sensing, organic chemists seeking for its photocatalytic ability resulting from

high energy electrons, electrical engineers who develop nano-optics, and biomedical engineers aiming to target and kill cancer cells.[1, 2] In bulk noble metal, the collective oscillation of conduction electrons, termed plasmon, plays an important role in optical and transport properties. A simple yet effective model, the Drude model, provides a lucid picture by treating conduction electrons as free electron gas. Within the Drude model, the response of conduction electrons to an external electric field can be obtained by solving the equation of motion of a single electron and multiplying by the electron density. The frequency dielectric constant, which is a measure of electric polarizability of a medium, has the following expression:

$$\varepsilon(\omega) = 1 - \frac{\omega_p^2}{\omega(\omega + i\gamma_b)} \qquad (1.1)$$

where ω is the optical frequency and γ_b is the bulk damping rate. The plasma frequency ω_p is given by $\omega_p = (Ne^2/\varepsilon_0 m_e)^{1/2}$, where N is the electron density, ε_0 is the vacuum permittivity, and m_e is the effective mass of the electrons.

For bulk noble metal, the Drude model well captures the experimental dielectric function in the near-IR region of spectrum (additional correction can be made by the empirical Drude-Lorentz model).[3] However, the Drude model breaks down in the visible and near-UV region due to the presence of inter-band transition of the electrons in d-orbitals.[4] For example, the onset of the inter-band transition is at 2.4 eV for gold (inset of Figure I.1) and 3.9 eV for silver. The inter-band transition gives a frequency dependent damping, and can be included in the dielectric function by adding an additional term:

$$\varepsilon(\omega) = \varepsilon^{ib} + 1 - \frac{\omega_p^2}{\omega(\omega + i\gamma_b)} \qquad (1.2)$$

Figure I.1 shows a plot of the real (ε_1) and imaginary (ε_2) components of the dielectric constant for bulk gold, where the low frequency response has been fit to the Drude model using Eq. 1.1.[1] It is noted that the ε_2 is related to damping, and the presence of inter-band transition causes a significant increase in damping at energies greater than 2.4 eV.

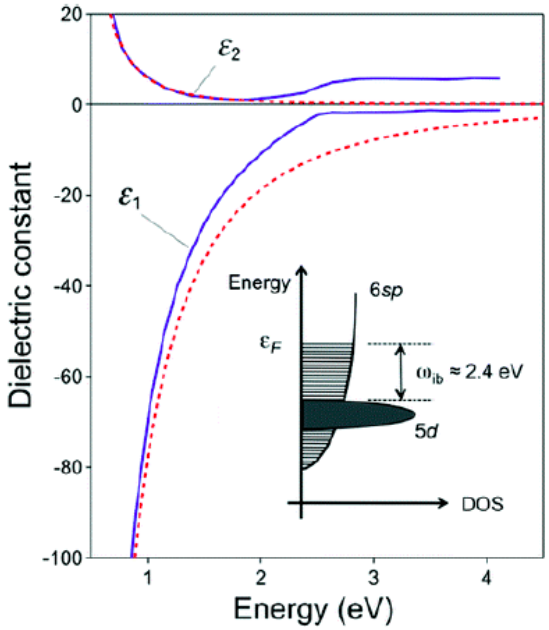

Figure I.1: Real and imaginary part of dielectric constant of gold. The dashed lines show a fit to the data using the Drude model (Eq. 1.1). The inset shows the band structure of gold. Reprinted in part with permission from G.V. Hartland. Optical Studies of Dynamics in Noble Metal Nanostructures. *Chemical Reviews*, **2011**, *111* (6), 3858-3887. Copyright 2011 by American Chemical Society.

The discussion above is applied in bulk noble metal. In noble metal nanostructures, the plasmon is confined in a geometry of a size comparable to or smaller than the wavelength of light, and this type of plasmon is called localized surface plasmon. An

important effect of the localized surface plasmon is the plasmonic enhancement: large fluctuations of charge densities are concentrated at "hot spots" near the surface of resonant geometries, thus the electric filed strength can be enhanced order of magnitudes. This plasmonic enhancement has a maximum at the localized surface plasmon resonance (LSPR) frequency. Because the LSPR is strongly dependent on the size, shape and surrounding environment, it offers a versatile platform for application such as plasmon-enhanced nonlinear optical process,[5] photovoltaics,[6] sensing[7] and photocatalysis.[8]

The dephasing time of localized surface plasmon, which refers to how fast the collective oscillation decay, is an important factor determining the plasmon enhancement factor and transport properties. Fast decay of localized surface plasmon leads to a short lifetime of coherent LSPR, which can limit some LSPR-based applications. Several plasmon dephasing pathways include radiative decay, observed as photon scattering, or non-radiative decay, observed as photon absorption which is followed by the generation of hot carriers, or loss as heat dissipation.[9] Presence of the adsorbed chemical species on the interface can also modify the plasmon dephasing pathway.[10] All these plasmon dephasing pathway can add up and be included in the damping constant in Eq. 1.2 to modify the $\varepsilon(\omega)$. In order to optimize the LSPR-based applications, strategies for manipulation and prolongation of LSPR dephasing time are desired. Besides optimizing material synthesis or nanostructure fabrication process,[11, 12] excitation of dark plasmon mode[13, 14] and introducing strong coupling to other resonance mode[15] were shown to prolong LSPR dephasing time effectively. Recently, there were emerging interest in using external stimulus such as magnetic field to modulate LSPR response.[16, 17] Two plasmon

modes with dipole perpendicular to the magnetic field evolve into two magnetic-field dependent collective modes, termed surface magnetoplasmon, which have dephasing time depending on magnetic field strength as well.[18]

1.3.2 Introduction to Faraday Effect in Plasmonic Nanostructures

Magneto-optical (MO) effect is a phenomenon that the polarization or the intensity of light is altered when passing through or reflecting from a magnetically ordered or magnetized material. MO phenomena provide abundant physical information of spin[19, 20] and electronic structures[21-23] of materials, and have found potential application in magnetic field sensors, displays, fast optical modulation, magnetic storage and optical isolators.[24] MO effect in most medium are typically small, therefore, it is essential to seek strategies to enhance MO effect, for which there are several methods. One of the strategies is to utilize strong near-field enhancement provided by plasmonic nanostructures. This approach provides a new route for modern photonics as the optical properties is controlled by geometrical resonance instead of the material property itself. Fruitful examples of implementation of this method have demonstrated considerable enhancement of MO activity.[25]

Faraday effect is one of the MO phenomena, which manifesting itself in an optical rotation of the polarization plane of linearly polarized light as it propagates along a magnetized medium (Figure I.2a). In such medium, the refractive index of left- and right-handed circularly polarized light is different due to the presence of magnetic field, therefore they propagate at a different speed. The optical rotation, $\Delta\theta$ is proportional to

the speed difference. The relation between optical rotation and external magnetic field strength can be expressed as

$$\Delta\theta = \upsilon \vec{B}_{app} L \quad (1.3)$$

where $\Delta\theta$ is Faraday rotation angle, $\vec{B}_{app}$ is the applied magnetic field, υ is the Verdet constant which is material dependent, and L is the effective travel distance of light inside the medium.[26]

The Faraday effect in bulk noble metals is typically small. For example, the polar reflection Faraday rotation of a gold thin film under 1 Tesla is only 2.8×10^{-9} degree.[23] However, in gold and its hetero-nanostructures, plasmonic enhanced Faraday rotation was observed.[27-30] The Verdet constant of nanocomposite of metal nanoparticles, such as dilute nanoparticle solution or embedded in dielectric medium, has been shown to have a resonance behavior at LSPR.[16] The resonance wavelength of the Verdet constant can also be tuned by the volume fraction and composition of nanoparticles.[27, 31] A clear example of plasmon enhanced Faraday rotation in 100 nm diameter gold nanoparticles (AuNP) colloid is shown in Figure I.3.[32] The spectral-resolved Faraday rotation reflects the contribution of a plasmon resonance feature also observed in the extinction spectra, near 575 nm. Deviations between the extinction and the Faraday rotation result from the spectral overlap of the Au 5d-6s interband transition, which has also been observed, for example, from samples of Au-coated iron oxide nanocrystals.[28] As reported by several others,[30, 33, 34] this trend indicates that Faraday rotation is strongly enhanced in metal nanoparticles.

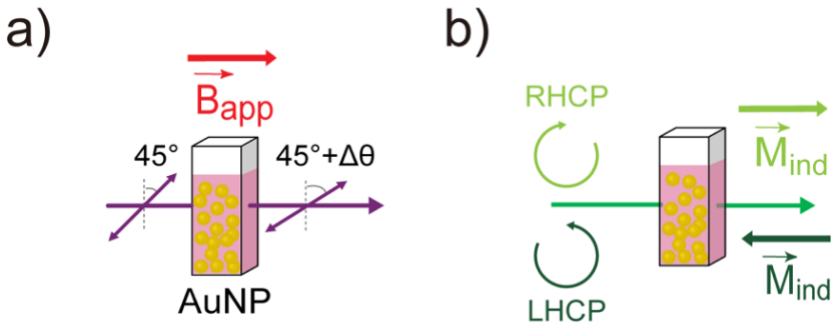

Figure I.2: Schematic of the Faraday effect and the inverse Faraday effect in gold nanoparticle colloids. (a) The Faraday effect is the rotation of the polarization plane of light transmitted through a magnetized medium. (b) The IFE is the induced magnetization of a medium.

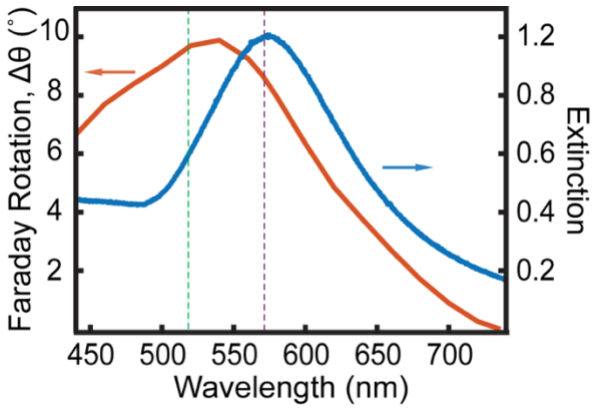

Figure I.3: Static Faraday rotation of 100 nm diameter AuNPs. Extinction spectrum (blue) and Faraday rotation spectra (red). Dashed lines indicate the pump (green) and probe (purple) wavelength used in time-resolved pump-probe experiment.

1.3.3 Introduction to the Inverse Faraday Effect in Plasmonic Nanostructures

In contrast to the Faraday effect, Inverse Faraday effect (IFE) manifests as an induced magnetization, $\vec{M}_{ind}$, that is parallel or anti-parallel with the axis of circularly

polarized excitation based on the helicity of the radiation (Figure I.2b). This induced magnetization can be described by:

$$\overrightarrow{M}_{ind} = \frac{\lambda \upsilon}{2\pi c}(I_{RHCP}\text{-}I_{LHCP}) \qquad (1.4)$$

where λ is the wavelength of light in vacuum, c is the speed of light, and I_{RHCP} (I_{LHCP}) is the intensity of right- (left-) handed circularly polarized light.

The IFE was first proposed as a reciprocal consequence of the conventional Faraday effect,[35] and both effects can be related through the same Verdet constant in Eq. 1.3 that describes Faraday rotation. The IFE has been studied extensively in materials with large Verdet constants, such as $Tb_2Ti_2O_7$ and $Ta_3Ga_5O_{12}$ for application in optically-written magnetic hard drives.[36, 37] In addition, strong resonant field concentration from plasmonic metasurfaces interfaced with these materials can further enhance sub-wavelength magnetization.[38] Note that the magnetization induced by the IFE is DC magnetic response, in stark contrast to the AC optical magnetic resonance in "artificial optical magnetism" community.[39]

While the IFE is a general term describing photo-induced magnetization under circularly polarized light, the origin of this magnetic response is distinct in different medium.[40] In plasmonic systems, Hertel showed that a simple classical microscopic model of the IFE can be obtained by separately considering oscillating and time-averaged contributions to electron motion in the continuity equation for a plasma subject to circularly polarized radiation.[41] The time-averaged current density can be written as:

$$\langle j \rangle = -\frac{i}{4e\langle N \rangle \omega} \nabla \times [\sigma^* \hat{E}^* \times \sigma \hat{E}] \qquad (1.5)$$

Where e is electron charge, $\langle N \rangle$ is time-averaged electron density, σ is electrical conductivity, $\hat{E}$ is the amplitude of an oscillating electric field, $\delta E(x,t) = \hat{E}\exp(ikr - i\omega t)$, where k is the wave vector. In the case of a circularly polarized excitation, $\hat{E} \times \hat{E}^* = \pm|E|^2 \cdot e_z$, while it is zero for linearly polarized excitation. The plus and minus sign refers to LHCP and RHCP, respectively. Eq. 1.5 shows that a DC circular current can be generated in plasmonic materials under circularly polarized illumination, and its direction is dependent on the handedness of light. The first term of Eq. 1.5 has the form of a solenoidal magnetization current j_M:

$$j_M = \nabla \times \vec{M}_{ind} \quad (1.6)$$

Hence, the light-induced magnetization $\vec{M}_{ind}$ generated in plasmonic materials is

$$\vec{M}_{ind} = \frac{i\varepsilon_0 e \omega_p^2}{4m\omega^3} [\hat{E} \times \hat{E}^*] \quad (1.7)$$

And the direction of $\vec{M}_{ind}$ also depends on the helicity of incident circularly polarized illumination.

Additionally, Hertel *et al.* also predicted a macroscopic drift current if there is optical field gradient presented in the material, providing an extra contribution to the induced magnetic field.[42] These two types of current density were demonstrated computationally by Athavan *et al.* using numerical approach in combination with full-wave optical simulations (Figure I.4a).[43] In a 100 nm diameter AuNP, they tracked the trajectory of individual electron subjected to circularly polarized illumination (Figure I.4b). They found that each electron moves in a solenoid-like path during an optical cycle, and the trajectory is lopsided owing to the optical field gradient inside the metal. The

lopsided electron trajectory produces a slower net drift current, which has the same helicity as incident light. Both solenoidal electron motion and drift current generate magnetic field in the same direction, with the former contribution dominant.

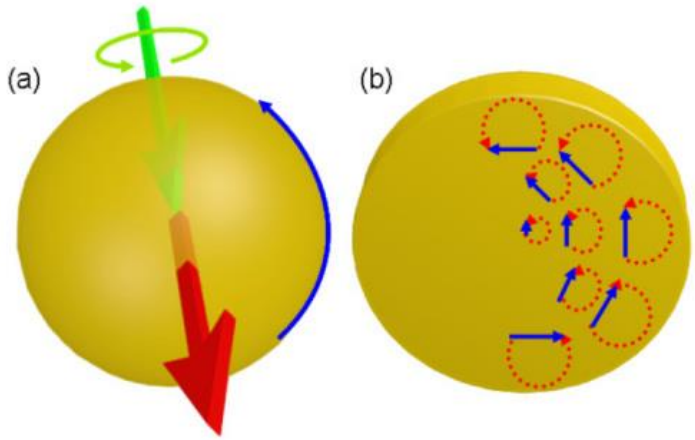

Figure I.4: (a) A 100 nm diameter AuNP under circularly polarized illumination (green arrow) will generate a static magnetic field (red arrow) along the optical axis, as well as circulating drift currents (blue arrow) due to the IFE. (b) A schematic illustration in cross section shows solenoid-like paths for individual electron (red dotted arrows) due to the forces experienced during the optical cycle. The trajectory is lopsided due to optical field gradients inside the metal, producing a net drift current (blue arrows). Reprint in part with permission from A. Nadarajah and M. Sheldon. Optoelectronic phenomena in gold metal nanostructures due to the inverse Faraday effect. *Opt. Express*, **2017**, *25*, 12753-12764. Copyright 2017 by The Optical Society.

While the above discussion is entirely within the framework of classical electrodynamics of continuous media, the light-induced magnetism was also predicted by various groups using classical approach[44] and more sophisticated computational method such as *ab initio* theory,[45] quantum hydrodynamic model[46] and DFT calculation.[47] Despite these intriguing predictions, direct experimental observation of the magnetic field due to

the IFE in plasmonic nanostructures has not been reported, with no time-resolved studies until now.

1.3 Introduction to Lead-Halide Perovskite Nanocrystals

1.3.1 Lead-Halide Perovskites Overview

Lead-halide perovskites (LHP) are emerging as one of the most promising materials for optoelectronic and solid-state lightening technologies. Perovskites have crystal structure with formula ABX_3, where A site is an inorganic or organic monovalent cation such as Cs^+, $CH_3NH_3^+$ (MA^+) and $CH[NH_2]_2^+$ (FA^+), B site is Pb^{2+}, X site is a halide anion such as Cl^-, Br^-, I^-. The variation of these chemical composition leads to highly tunable photophysical properties.[48]

The upsurge of research interest in LHP originated from its huge potential in photovoltaic application.[49] Used as a sensitizing material in photovoltaic devices, the efficiency of LHP-based single junction solar cell has reached over 25% in just a decade of development, which surpass the long-established organic dye molecule and almost catch up with single crystal Si cell.[50] The high photovoltaic efficiency of LHP thin film can be attributed to its ability to absorb photon efficiently, meaning that the materials have large absorption coefficient. In fact, $CH_3NH_3PbI_3$ showed an absorption coefficient more than one order of magnitude greater than that of silicon and conventional molecular dye.[51, 52] A large absorption coefficient also contributes to a large open-circuit voltage of solar cell. After a photon is absorbed, the photo-excited charge carrier has to be extracted. During this process, there are several energy loss pathways such as carrier trapping,

radiative recombination, and exciton formation. While charge extraction is a complicated process, several parameters can be used to quantify the performance of carrier extraction such as carrier lifetime, carrier mobility and carrier diffusion length. LHP thin film possess superior performance in all these parameters: carrier mobility over 25 cm^2/Vs, diffusion length over 1μm, and long carrier lifetime over 1 μs.[51, 53] In addition, the ability to process at low temperature and in solution makes LHP a cost-effective material system comparing to other solar cell materials. These exciting properties make LHP a hot material system in photovoltaic community.

Besides in the photovoltaic community, LHP also raised a lot of interest in the solid-state lightening community.[54-57] LHP not only possesses large absorption coefficient, but also emits photon efficiently, meaning that it has high photoluminescence (PL) quantum yield (QY) – which can easily reach 80% after solution processing and up to 100% after careful surface treatment. Nonradiative pathway such as carrier trapping is suppressed in the LHP due to its defect-tolerant electronic structure.[58] Furthermore, the highly deformable lattice leads to a strong coupling between charge carrier and lattice vibrational mode, resulting in the formation of polaron, which is suggested to protect charge carriers from scattering with localized defect.[53]

Despite the excellent optoelectronic and photonics properties of LHP, the most significant problem for the practical application is the instability in ambient condition and under high excitation density. Due to the ionic nature of the crystal, the LHP is highly soluble in polar solvent and can be easily destroyed by humidity, especially under illumination.[59-61] Excess heating, such as excess Joule heating in light-emitting diode due

to long-time illumination, accelerates ion migration and material degradation, which introduce high density of defects that increase nonradiative recombination. Furthermore, upon continuous illumination, initially homogeneous mixed LHP undergo spontaneous separation. Low bandgap states form and act as trap state, which is detrimental to photovoltaic devices performance.[62, 63] Studies focused on material engineering and optimizing device geometry is a vigorous field to improve the stability and prolong the lifetime of LHP-based devices.[64, 65]

1.3.2 Strongly Quantum Confined Lead-Halide Perovskite Nanocrystals

Perovskites were firstly prepared as thin film, but now they are also available as nanocrystals (NCs) with confinement in different dimension, such as nanoplatelets, nanowires and quantum dots (QDs).[66] LHP NCs have attracted tremendous attention for several reasons: The synthesis is facile and the yields are high, the bandgap can be tuned via post-synthesis treatment, and the QY can reach 100% after surface ligand treatment.[67-69]

In this dissertation, QDs will be specifically discussed. In general, QD is described as the size of NCs smaller than twice of Bohr radius, a_B. In this size regime, the optical and electronic properties are affected by spatial confinement of the carrier wavefunctions. The confinement range can be further divided into strong, intermediate and week confinement regimes which corresponds to a size range of $a << a_B$, $a \sim a_B$, $a >> a_B$. Semiconductor QDs exhibit size tunable properties that offers a diverse platform to study the confinement effects in quantum systems in a size range between bulk and

atomic/molecular system. While many papers have been published in the last few years to study the photophysical properties of LHP QDs, many papers were plagued by problems such as sample inhomogeneity in both size and shape distribution. Recent synthetic progress in LHP QDs utilizing thermodynamic equilibrium for the precise size control in strongly confined regime, enabling the exploration of the unique photophysical properties of LHP QDs unambiguously.[70]

For example, fundamental determination of absorption cross section, which is an important parameter for lasing and photocatalysis application, of LHP QDs were measured. While the absorption cross section value were provided by several other reports, these values were scattered.[71, 72] Puthenpurayil *et al.* used transient absorption in combination of inductively coupled plasma mass spectrometry (ICP-MS) analysis and provided an empirical volume law for determining absorption cross section of $CsPbBr_3$ QDs.[73]

Another example is regarding the determination of electronic fine structures of LHP QDs. While the nature of ground state of LHP QDs has been a debate in the last several years,[74-76] Rossi *et al.* studied time-resolved photoluminescence from strongly confined LHP NCs and observed intense dark exciton emission in cryogenic temperature.[77, 78] Their result provides a direct proof of dark exciton as ground state in the strongly quantum confined NCs, while this effect is not observed in the nonconfined one. A long lifetime of ground state dark exciton could be attractive to many applications such as photocatalysis which required long lived charge carrier to generate highly energetic photoelectron.[79]

Similar to their bulk counterpart, LHP QDs are promising in photonics application.[80-82] In addition to chemical composition, LHP QDs offer additional degree of freedom to tune the emission wavelength through size and avoid halide segregation. In this dissertation, studies on PL wavelength and linewidth, and their dependence on size and temperature will be discussed in detail.

CHAPTER II

LIGHT INDUCED MAGNETISM IN GOLD NANOPARTICLES[1]

2.1 Introduction

Strategies for ultrafast optical control of magnetism have been a topic of intense research for several decades because of the potential impact in technologies such as magnetic memory,[83] spintronics,[84] and quantum computation, as well as the opportunities for non-linear optical control and modulation[85] in applications such as optical isolation and non-reciprocity.[86] The IFE has been shown to be a promising approach to manipulate magnetism in dielectric materials with large Verdet constant.[36, 87] However, there has been limited research studying magnetization that occurs within non-magnetic plasmonic metals due to the IFE, without other magnetic structures, despite compelling theoretical studies that suggest plasmonic nanomaterials may out-perform more conventional magnetic materials in terms of induced magnetic field strength, spatial confinement, ultrafast time response, and other technologically relevant optoelectronic behavior.[41, 43, 46, 88] Several studies have also reported anomalously large Verdet constants in plasmonic colloids, that we confirm below, further suggesting strong enhancement of the IFE may also be possible.[28, 34]

For example, as opposed to the traditional phenomenological analysis that treats the IFE as a nonlinear four-wave mixing process,[89, 90] Hertel recently derived an intuitive

[1] Reprinted in part with permission from "Light-induced magnetism in plasmonic gold nanoparticles" by Oscar Hsu-Cheng Cheng, Dong Hee Son, Matthew Sheldon. *Nat. Photonics*, **14**, 365–368. Copyright 2020 by Springer Nature.

microscopic model based on the continuity equation for an electron plasma subject to circularly polarized light.[41] The light-induced magnetization is interpreted as resulting from the solenoid-like path traced out by each electron subjected to the rotating electric field during an optical cycle. Additionally, our laboratory has recently performed computational analyses of the IFE in plasmonic gold nanoparticles building from Hertel's approach.[43] Our calculations predict pronounced macroscopic drift currents that circulate the exterior of nanoparticles normal to the incident beam, in addition to the coherent solenoid-like motion of all electrons at the optical frequency.[42] Moreover, these associated phenomena of the IFE are enhanced in nanoparticles compared with bulk films, due to resonant optical concentration at plasmonic hot spots and, separately, an enhanced Verdet constant resulting from the electronic behavior of the confined geometry.[34, 41, 43, 91] Indeed, a recent theoretical study using a quantum hydrodynamic model predicted the generation of magnetic moments exceeding 1 μ_B per gold atom in 2 nm diameter gold nanoparticles.[46] This mechanistic picture of the light-induced magnetization is also predicted by *ab initio* calculations that show circularly polarized optical fields driving the coherent motion of the electron gas, with magnetization resulting from the induced orbital angular momentum of electrons.[45] Because spin alignment of individual electrons does not contribute to the mechanism, the magnetization is expected to be instantaneously synchronized with an optical pump, in contrast with dynamics that are limited by spin-spin or spin-lattice relaxation times typical in ferromagnetic materials.[92,93] Despite these intriguing predictions, measurements of the magnetic field due to the IFE in plasmonic nanoparticles has not been reported, with no time-resolved studies until now.

In order to measure induced magnetization in plasmonic gold nanoparticles produced by the IFE, we performed static and ultrafast pump-probe Faraday rotation measurements on 100 nm AuNP colloid. First, the spectrally resolved Verdet constant was determined from static Faraday rotation measurements on the sample colloid solution in a 1 cm-pathlength cuvette. On the same sample in a 2 mm-pathlength flowing cell, the IFE was induced by a circularly polarized pump beam. The resultant magnetization was indicated by the Faraday rotation angle ($\Delta\theta$) of a linearly polarized probe beam. Based on the previously measured Verdet constant, the magnitude of the optical rotation of the probe thus enabled quantitative determination of the strength of the induced magnetization.

2.2 Result and Discussion

The Verdet constant extracted at the concentration of AuNP in this study is 43.3 $rad \cdot T^{-1}m^{-1}$ at 575 nm (Figure II.3), which is about half that reported for the strong Faraday rotator materials such as terbium-doped boron-silicate glasses,[94] and it is 16 times larger than bulk gold per unit length of metal.

An ultrafast pump-probe Faraday rotation measurement quantified the induced magnetic field via the IFE. In this detection configuration, besides the optical rotation induced by the IFE, the optical Kerr effect (OKE) also caused rotation of the linearly polarized probe beam. The separate contribution of the OKE and IFE were disentangled by examining the dependence on polarization angle difference between the pump beam and the probe beam, δ, and the ellipticity angle of the pump beam, ϕ, respectively. The definition of these parameters is shown in Figure II.1. The total induced rotation, $\Delta\theta$, from

the combined effects of the IFE and the OKE depend on $\chi^{(3)}_{xxyy}$ and $\chi^{(3)}_{xyyx}$ of the third-order susceptibility as given by[95]:

$$\Delta\theta = [\mathrm{Im}(F_+)\cdot\cos(2\phi)\cdot\sin(2\delta) + \mathrm{Re}(F_-)\cdot\sin(2\phi)] \qquad (2.1)$$

with the contributions from the IFE and the OKE labeled as F_- and F_+, and

$$F_\pm = \frac{-32\pi^3 L I_P}{\lambda_{pump} c|1+n|^2}\left(\frac{\chi^{(3)}_{xxyy} \pm \chi^{(3)}_{xyyx}}{n}\right) \qquad (2.2)$$

Where I_P is the pump intensity, λ_{pump} is the pump wavelength, and n is the refractive index.

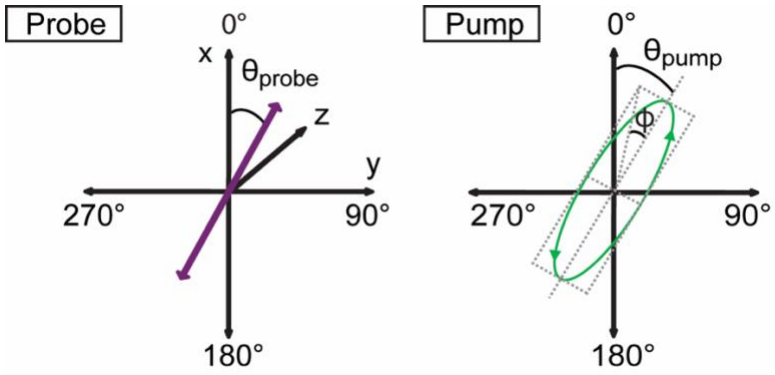

Figure II.1: Definition of the coordinate system and corresponding variables in IFE experiment. Light propagation is along the z-axis in the positive direction. The probe beam is linearly polarized for all experiments, with polarization angle θprobe. The pump beam can be linearly, elliptically, or circularly polarized. The polarization angle of the pump beam (when linearly polarized) or azimuth angle (when elliptically polarized) is θ_{pump}. The difference between θ_{probe} and θ_{pump} is defined as $\delta = \theta_{probe} - \theta_{pump}$. The ellipticity angle, ϕ describes the extent of circular polarization of the pump and takes positive values when right-handed and negative values when left-handed.

In this experiment, two cases with different δ were assigned. In Case I (δ = 45°), we observed Δθ is predominately due to the OKE (red dots in Figure II.2b). In Case II (δ = 0°), $\Delta\theta = \mathrm{Re}(F_{-}) \cdot \sin(2\phi)$, indicating that Δθ is purely the result of the IFE (blue dots in Figure II.2b). In Case II, with increasing ellipticity of the pump, the signal increases and a positive and negative maximum are observed when the pump is either purely left-hand (LHCP) or right-hand circularly polarized (RHCP). This dependence on the helicity of the pump is an important criterion for confirming the presence of the IFE, consistent with Eq. 1.7. Further, the ellipticity-dependent studies (Figure II.2b) demonstrate a very clear difference between the signal from Case I experiments and Case II experiments.

The time response of the IFE is shown in Figure II.2c. We observe a single peak for any ellipticity of the pump, and this is in contrast with reports of Au thin films that show a bipolar shape of the time response at some elliptical pump excitations.[96, 97] In addition, the time response appears to be limited by the pump-probe cross correlation, indicating an instantaneous magnetization and demagnetization process within the sub-picosecond time resolution of our experiment. While similar ultrafast demagnetization behavior has also been observed in other metal thin films,[92, 97, 98] this behavior is in stark contrast to the optically-induced dynamic magnetism in ferromagnetic metal films and magnetic nanocrystals,[92, 99] where ultrafast demagnetization is followed by much slower hysteretic remagnetization. The time response observed here is consistent with a mechanism of coherent transfer of angular momentum from the optical field to the electronic motion, in agreement with the *ab initio* calculations discussed above.[45]

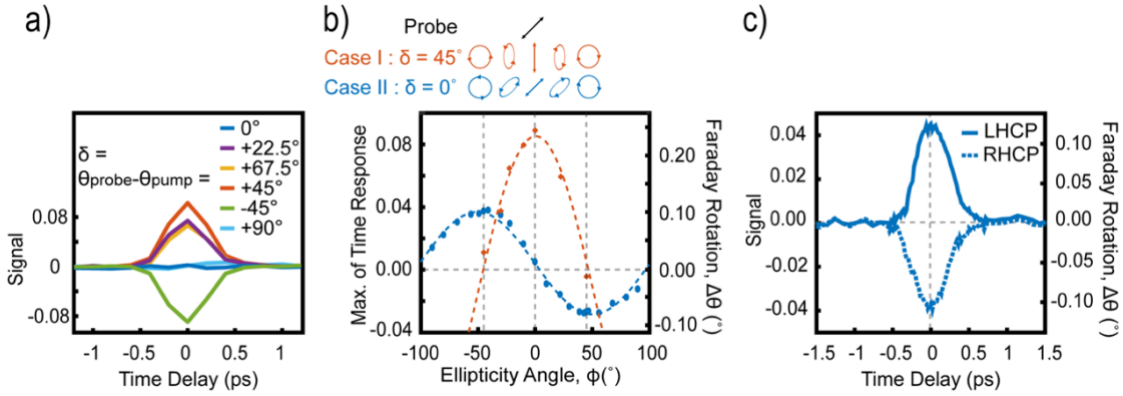

Figure II.2: Time-resolved pump–probe IFE experiment on 100 nm diameter AuNPs. (a) Light-induced rotation due to only the OKE ($\phi = 0°$), as a function of δ. (b) Light-induced rotation as a function of ϕ. Red dots represent data from experiments with the geometry of Case I, where $\delta = 45°$. Blue dots represent data for the Case II geometry, where $\delta = 0°$. Dashed lines are fits to the data. (c) Light-induced rotation due to pure IFE when the pump is LHCP ($\phi = -45°$, solid line) or RHCP ($\phi = +45°$, dashed line), corresponding to the positive and negative maxima for Case II in (b). A small OKE background signal at the same quarter-waveplate rotation is subtracted. We believe that minor deviations from a pure IFE signal in the Case II geometry is due to imperfect alignment of the pump and probe beam along the sample axis.

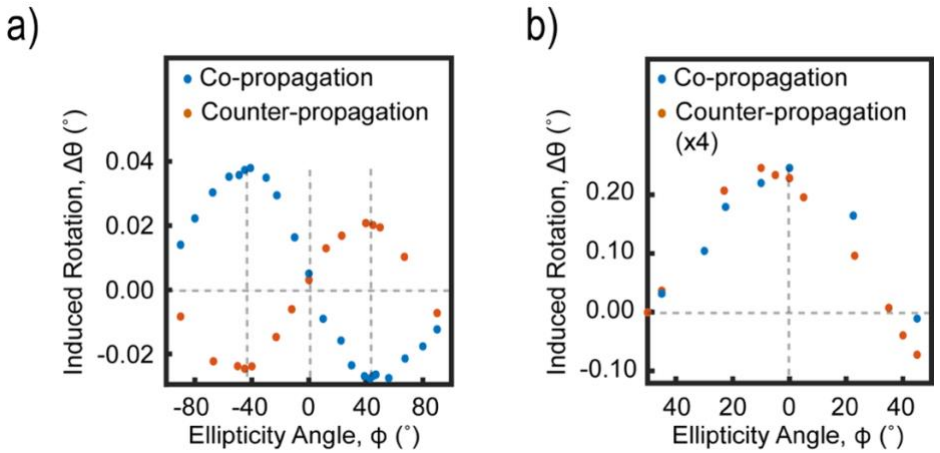

Figure II.3: IFE experiment with counter-propagating pump and probe beams. (a) Case II configuration. The induced rotation has opposite sign when the pump beam is counter-propagating. This result demonstrates non-reciprocal Faraday rotation of the probe beam, resulting from the optically pumped magnetization of the AuNP colloid due to the IFE. (b) Case I configuration. The induced rotation resulting from the OKE does not depend on the propagation direction of the pump and probe beams.

In order to further confirm a magnetic field was created during optical excitation, as opposed to other non-linear optical phenomena or photothermal heating that could contribute to the measured optical rotation, we also performed the IFE experiment with counter-propagating pump and probe beams. In the polarization configuration of Case II (Figure II.3a), the induced rotation showed opposite sign when the pump beam was counter-propagated (red dots). The slightly smaller magnitude of rotation is due to a smaller effective increase of the pump-probe cross correlation in the counter-propagating configuration. However, in the configuration of Case I (Figure II.3b), the induced rotation does not depend on the pump beam direction. This result confirms that a transient change in refractive index of the material (OKE) or any other photothermal effects are reciprocal for either direction of the probe beam with respect to the pump beam. Importantly, in contrast, the IFE depends strongly on the propagation direction of the pump and probe beams, confirming the presence of the magnetization that gives rise to the nonreciprocal Faraday rotation of the probe beam.

The maximum induced optical rotation in the Case II configuration as a function of peak pump intensity is plotted in Figure II.4. The optical rotation shows a linear dependence, as predicted in Eq. 1.4 and Eq. 1.7, further confirming that the optical rotation is due to the IFE. The magnitude of induced magnetization, $\vec{M}_{ind}$, of the AuNPs during excitation can be determined by analyzing the measured Verdet constant and optical rotation in the pump-probe experiments (Appendix A.2):

$$\Delta\theta = \upsilon_{IFE}\vec{B}_{eff}L = \upsilon_{IFE}\mu_0\left(\frac{1}{\chi_v}+1\right)\vec{M}_{ind}L \qquad (2.3)$$

Here $\vec{B}_{eff}$ can be thought of as the strength of an externally applied magnetic field that would be required to induce the same optical rotation observed in the pump-probe measurement.[100] We observe $\vec{B}_{eff}$ up to 0.038 T at a peak pump intensity of 9.1×10^{13} W/m^2. The value of $\vec{M}_{ind}$ can be further analyzed to determine the magnetic moment of each Au nanoparticle. If we consider that the individual Au nanoparticles act as small bar magnets with rotation and diffusion that is much slower than the pulse duration, the ensemble response corresponds to an induced magnetic moment per particle of 2.9×10^7 μ_B or 0.95 μ_B per Au atom, where μ_B is the Bohr magneton (Appendix A.3). Note that the magnitude of the induced magnetic moment is not simply due to optical field concentration on the AuNP surface (~5×),[43] but also results from the larger Verdet constant of the nanoscale geometry (Appendix A.5).

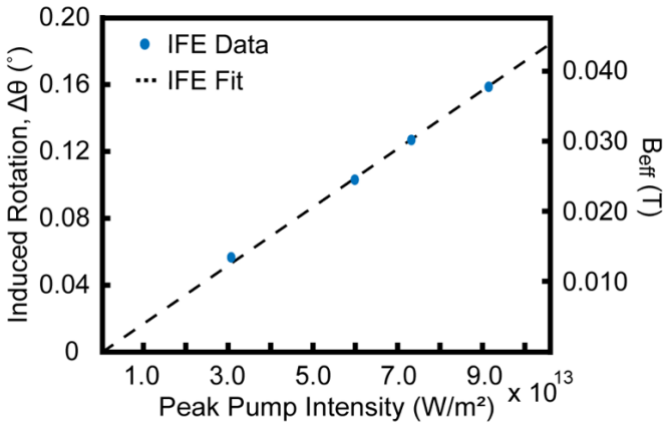

Figure II.4: Dependence of optical rotation on pump intensity for Case II and the corresponding effective magnetic field. The fit shows a linear trend. The optical rotation is the result of an effective light-induced magnetic field, B_{eff}, in the AuNPs.

2.3 Conclusion

In summary, we report the first experimental observation of optically-induced magnetization in Au nanoparticles due to the IFE. We distinguished the contribution of the IFE and OKE in the optical rotation signal of a pump-probe experiment by analysis of the polarization-dependence, and by confirming the optical non-reciprocity imparted by the magnetization due to the IFE. Furthermore, the time response indicates a distinct mechanism of photo-induced magnetism that results from the coherent circular motion of electrons, in contrast with the spin dynamics typical in ultrafast studies of ferromagnetic materials. Additionally, we observed optically induced magnetization due to both plasmonic field enhancement as well as changes to the intrinsic electronic response of the nanoscale geometry. We anticipate these results may be of great interest in the photonics community. For instance, recent reports have shown the ability to effectively control local magnetization in plasmonic heterostructures.[25, 38] Our experiments outline opportunities for studying the ultrafast optical control of magnetic properties in these individual sub-wavelength geometries, as well as the interplay between light-induced and permanent magnetization. We also envision applications in nanoscale all-optical methods of optical isolation that do not require externally applied magnetic fields.[85, 101]

2.4 Experiment Detail

2.4.1 Static Faraday Rotation Spectroscopy

Experiments were performed on colloids of 100 nm diameter AuNP in water (stabilized in sodium citrate, OD = 1 at 572 nm, volume fraction = 1.14×10^{-6}, Alfa Aesar).

The sample was placed in a 1 cm path length quartz cuvette. A static magnetic field (0.35 Tesla) was applied along the direction of a transmitted linearly polarized probe beam. A tungsten lamp was used as a light source, and the wavelength was selected by a monochromator (Newport, Model 74004). The beam was polarized by a sheet polarizer. A reference beam split by a reflective neutral density filter (OD = 0.2) was measured by a Si photodetector (Thorlabs, PDA100A). The Faraday rotation angle, $\Delta\theta$, was measured by sending the probe beam through Wollaston prism optically in-series with a balanced photodiode (New Focus, model 2307) after the beam had passed through the sample, and $\Delta\theta$ was calculated by the following equation: $\Delta I_{BPD}/I_{REF} = \sin(2\Delta\theta)$, where ΔI_{BPD} is power difference received at the balanced photodiode from the two polarized beams delivered by the Wollaston prism, I_{REF} is power measured by a referenced Si photodetector (Figure II.5). Note that $\Delta I_{BPD}/I_{REF} = \sin(2\Delta\theta) \approx 2\Delta\theta$ when $\Delta\theta$ is small. A lock-in amplifier (Stanford Research, SR830) was used to improve signal-to-noise ratio of the measurement.

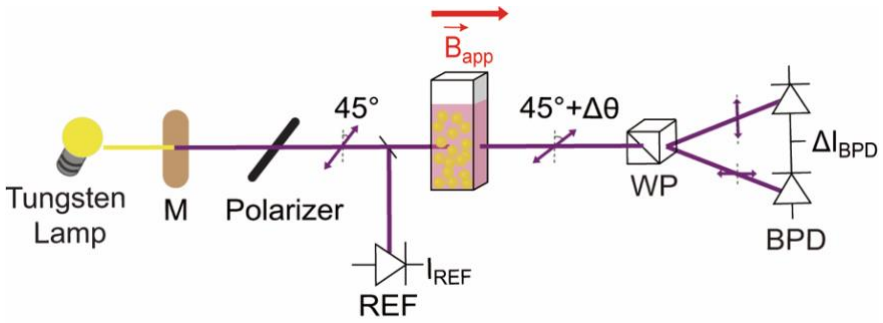

Figure II.5: Detailed schematic illustration of experiment setup. M, Monochromator; REF, Referenced Silicon photodiode; WP, Wollaston prism; BPD, Balanced photodiode.

2.4.2 Time-resolved Pump-probe Faraday Rotation Spectroscopy

Measurements were made using an amplified Ti:sapphire laser system (KM Labs) operating at a repetition rate of 3 kHz. The pump beam centered at λ = 515 nm (green dashed line in Figure I.3) was generated from a home-built double-passed noncollinear optical parametric amplifier system (NOPA). The probe beam was derived from a white light continuum generated in a translating CaF_2 crystal and the wavelength was selected using a chirp compensating prism pair and a spatial filter. A simplified scheme for optical setup is shown in Figure II.6.

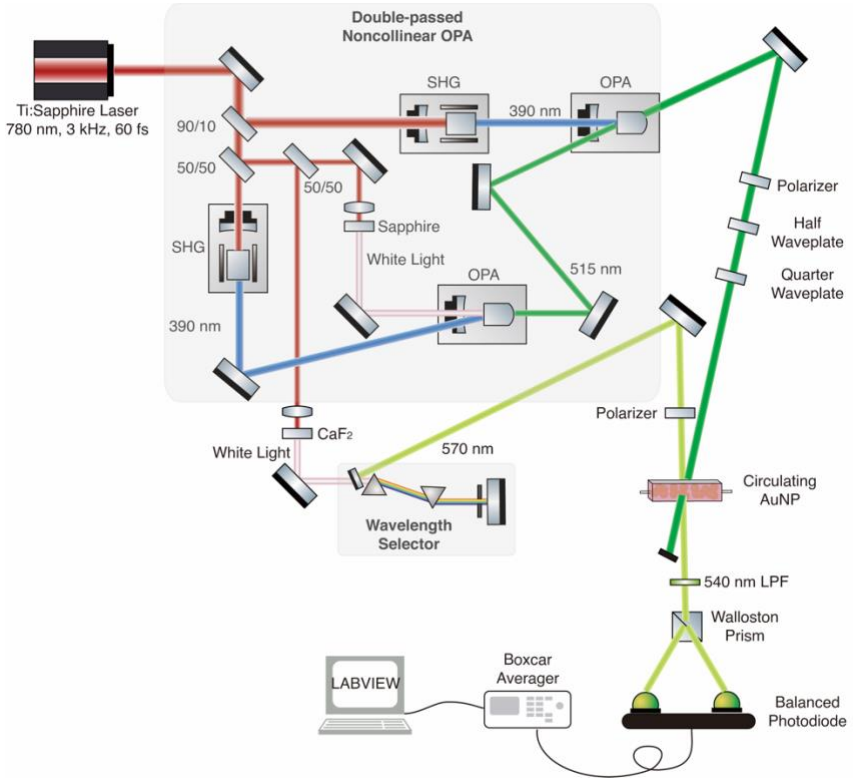

Figure II.6: Simplified scheme of optical setup for time-resolved pump-probe Faraday rotation spectroscopy. SHG, Second harmonic generation; OPA, Optical parametric amplifier; LPF, Long-pass filter.

The beam size (full width at half maximum, FWHM) of the pump and probe beam, which were measured by a CCD camera (The Imaging Source, DMK 21BU618), are 150 ± 6 μm and 80 ± 2 μm in diameter, respectively. The temporal resolution of the measurements was 0.53 ps, which was estimated by FWHM of the OKE signal of Au nanoparticle colloid (Figure II.7). During the experiment, the 100 nm diameter Au nanoparticle colloid was continuously circulated in a 2 mm path length quartz flow cell (Starna Cells, 45-Q-2) to prevent potential sample damage or accumulated thermal effects. The induced Faraday rotation of the probe beam by the pump beam was measured using the same configuration as in the static Faraday rotation experiment as a function of pump-probe time delay, but without an externally applied magnetic field. The signal measured by the photodiode was processed through boxcar averager (Stanford Research, SR250) and home built LABVIEW software. The induced Faraday rotation angle was calibrated by using the combination of a neutral density filter and a linear polarizer (Figure II.8).

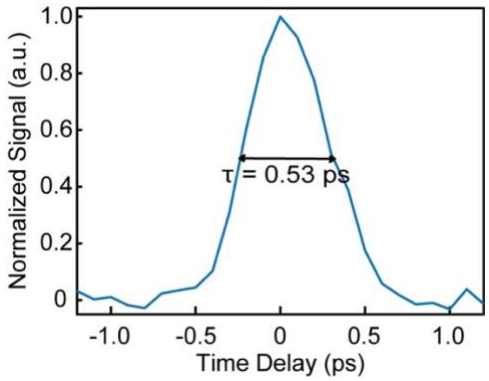

Figure II.7: Estimation of the pump pulse width from the OKE signal of the Au nanoparticle colloids. The OKE signal is treated as the cross-correlation of the pump and probe pulse, with full width at half maximum τ = 0.53 ps. Thus, we estimate the upper limit of pump pulse width to be $\tau/1.44$ = 0.37 ps, which is used to calculate peak pump intensity in Figure II.4.

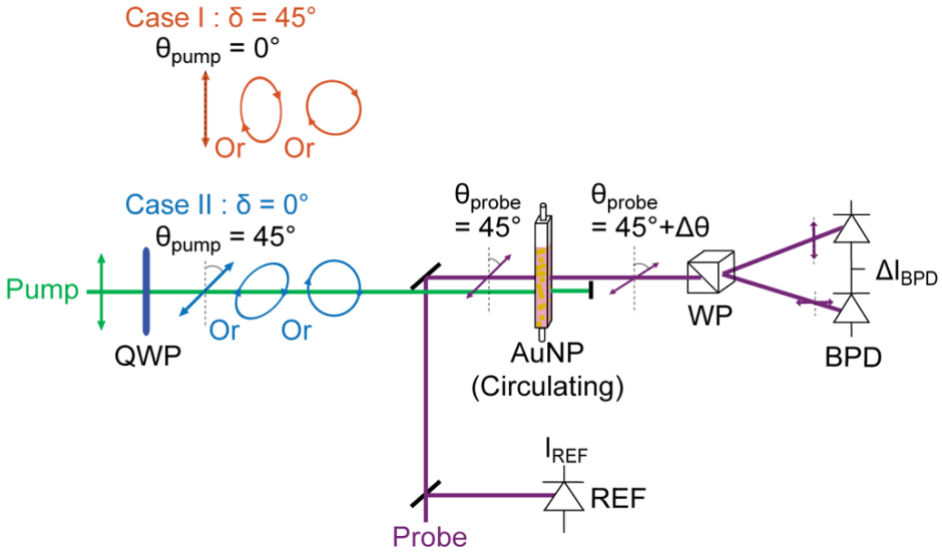

Figure II.8: Time-resolved pump-probe Faraday rotation spectroscopy. The induced Faraday rotation was calibrated using the combination of a neutral density filter (OD = 0.06) and a linear polarizer. First, the neutral density filter was placed in front of one side of the BPD, resulting in some ΔI_{BPD} output signal. Then a linear polarizer was placed between AuNP and WP and was rotated until the BPD was balanced. $\Delta I_{BPD}/I_{REF}$ signal is then calibrated by the ΔI_{BPD} output signal produced by the neutral density filter and linear polarizer rotation angle. QWP, Quarter wave plate.

CHAPTER III

PHOTOTHERMAL EFFECT MODULATION BY LIGHT ELLPTICITY IN GOLD NANODISKS ARRAY

3.1 Introduction

Strategies for manipulating magnetism using light has been an active research topic in recent years due to its potential in future information processing technologies[102, 103] as well as novel nanophotonic applications.[39] Experiments with circularly polarized femtosecond laser pulses have shown that effective magnetic field up to several Tesla can be generated in magnetic materials by coherently controlling the electron spin,[100] and this optomagnetic phenomenon is called the inverse Faraday effect (IFE). Furthermore, it has been suggested that this optomagnetic approach could be enhanced and mastered in nanoscale by integrating magneto-optical active materials with plasmonic nanostructures, which is known for its subwavelength spatial confinement and optical enhancement.[25] While in the field of magnetoplasmonics a magneto-optical active medium is always involved, studies have also shown that by properly engineering the morphology of plasmonic nanostructure, strong magnetic resonance can be induced. Sub-wavelength meta-molecules made from coupled gold nanoparticles can support circulating displacement current around the structure and generate strong AC magnetic response at optical frequencies.[104] Since gold is non-magnetic in nature, this phenomenon is also called “artificial optical magnetism”. In contrast to artificial optical magnetism, another approach to generate static magnetic field in plasmonic nanostructures by means of

circularly polarized light was shown conceptually[43] and experimentally.[32] A classical way to understand the origin of this light-induced DC magnetic field is the orbital angular momentum of individual circular electron motion coherent to an optical cycle (Eq. 1.5).[31, 41] Additionally, a drift current results from the presence of optical field gradient throughout the plasmonic nanostructures provides an additional contribution to the induced magnetic field.[42] This mechanism is also supported by more sophisticated computational method such as *ab initio* theory,[45] quantum hydrodynamic model[46] and DFT calculation.[47]

While the IFE in plasmonic nanostructures mentioned above is under the condition of high peak intensity femtosecond laser pulses excitation, several studies reported by Vuong group have suggested that the light-induced magnetic response can be observed under low intensity CW illumination.[88, 105] In their studies, the magnetic response was also attributed to a nonlinear DC circular current induced in AuNP only when the incident light is elliptical or circularly polarized. Notably, in the meanwhile, an anisotropic increase of the electrical conductivity as a consequence of this nonlinear DC circular current was predicted and attributed to the change in extinction spectra observed in their experiment (Figure III.1).[105] Based on the Drude model, the DC electrical conductivity, σ, is connected to plasmon dephasing time, $\tau_{dephase}$ through the following expression:

$$\sigma = \frac{Ne^2\tau_{dephase}}{m^*} \quad (3.1)$$

where m^* is effective mass of electron. The linear relation between σ and $\tau_{dephase}$ suggests that the plasmon dephasing time in AuNP also increases under circularly polarized illumination. Since $\tau_{dephase}$ is fundamentally connected to the dynamics of

plasmon, it proposes an appealing possibility to modulate optical and transport properties in a plasmonic nanostructures reversibly.

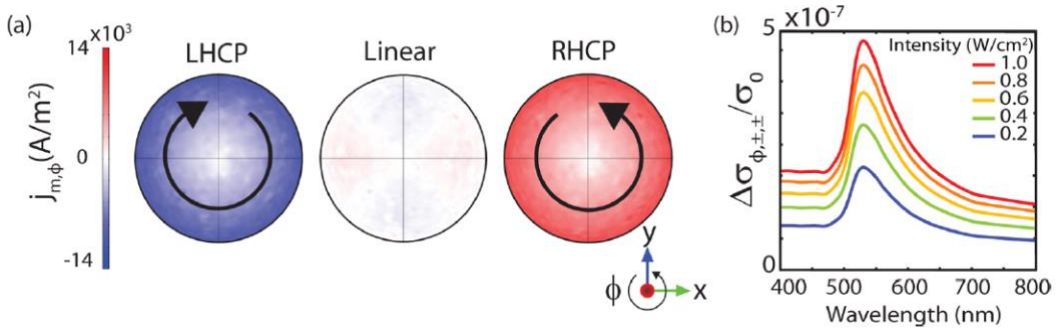

Figure III.1: (a) Surface plots of the nonlinear circular current density of an 80 nm gold nanosphere when illuminated by LHCP, linear polarized light and RCHP (b) Volume-averaged relative change in azimuthal component of the DC electrical conductivity as a function of wavelength when illumination intensity is varied for RHCP or LHCP. Reprint in part with permission from M. Moocarme, J. L. Domínguez-Juárez, L. T. Vuong. Ultralow-Intensity Magneto-Optical and Mechanical Effects in Metal Nanocolloids. *Nano Letters*, **2014**, *14* (3), 1178-1183. Copyright 2014 by the American Chemical Society.

The ability to reversibly modulate plasmon response in a plasmonic nanostructures using external stimulus is of great interest in active plasmonic community for potential application such as plasmonic sensing and tunable surface-enhanced Raman scattering.[106] An electrical field can be used to alter the charge carrier density in materials, along with changes in their dielectric function. However, in pure plasmonic metal the electrical conductivity modulation using DC electric field is usually imperceptible owing to the high density of conduction electron screening. For instance, a tiny DC electrical conductivity modulation of $\Delta\sigma = 0.1\%$ in a 10 nm gold thin film when electric field of 10^6 V/cm was

applied.[107] However, instead of applying DC electric field, AC electric field can in principle introduce time-varied local change in the surface charge density, producing pronounced electrical conductivity modulation. For example, a recent study using THz field to induce local change of surface charge density in gold microparticle demonstrated $\Delta\sigma$ up to 46% .[108] While the timescale in this study was in ps timescale, the results from the Vuong group in gold nanoparticle provided an appealing possibility to modulate DC electrical conductivity and plasmon response under CW excitation.[88, 105]

In this study, we aim to expand the observation from the Vuong group and provide an experiment proof of anisotropic change of the electrical conductivity in a gold nanodisks array. Temperature was used as an indicator of electrical conductivity change since Joule heating resulting from the light-induced circular current is linear proportional to electrical conductivity:

$$p = \sigma E^2 \qquad (3.2)$$

where p is the power generated through Joule heating and E is electric field. By using Raman thermometry, both nanostructure temperature and plasmon dephasing time information can be extracted.

3.2 Result and Discussion

Gold nanodisks array sample was prepared by electron-beam lithography method. The choice of gold nanodisks array was because of several reasons: First, the geometry of the structure has to be in circular shape in order to support circular plasmon mode under circularly polarized excitation. Second, a periodic nanodisks array instead of isolated or

randomly distributed nanodisks was preferred because it has high absorptivity in visible range, which maximize the photothermal effect we aimed to probe (Figure III.2).[109]

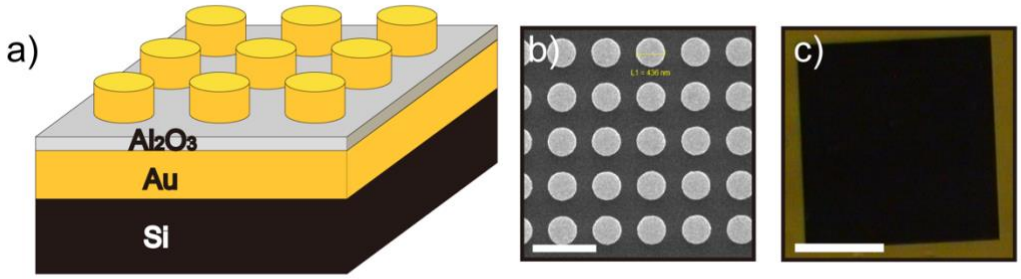

Figure III.2: Gold nanodisks array sample. (a) Illustration of gold nanodisks array sample (not to scale) (b) SEM image (c) Optical image, the black area is gold nanodisks array. Scale bar is 1 µm and 40 µm, respectively.

Raman thermometry method was used to quantify the photothermal effect. Traditionally, in a substrate with distinct vibrational mode, such as bare silicon, its temperature can be obtained from the ratio between Stoke and anti-Stoke signal of a given Raman band.[110] However, the electronic Raman signal observed in plasmonic substrate is usually a broad band (Figure III.3a), thus this method is not valid. On the other hand, it is commonly observed that a bi-exponential decay of the anti-Stoke Raman signal from plasmonic metals is strongly temperature dependent.[111, 112] Several studies have proposed that the anti-Stoke spectrum of plasmonic metals can be fitted to extract the lattice temperature of the metal, T_l, the elevated electronic temperature, T_e, and the size of the

sub-population of hot carriers, α, in the steady state.[113-115] Furthermore, a model developed recently by our group successfully described the entire Stokes and anti-Stoke Raman signal, by taking into account additional contribution from non-thermal carriers with an energetic distribution dependent on plasmon dephasing time $\tau_{dephase}$.[116] The overall Raman spectrum, which is scaled with joint density of state $J(\hbar\omega)$,[117] can be described according to the following expression:

$$J(\hbar\omega) = D \cdot R \cdot \begin{bmatrix} \int L\left(E,\tau_{dephase}\right) f(E,T_l) L\left(E+\hbar\omega,\tau_{dephase}\right)\left(1-f(E+\hbar\omega)\right)dE + \\ \alpha \int f(E,T_e)\left(1-f(E+\hbar\omega,T_e)\right)dE \end{bmatrix} \quad (3.1)$$

where D is a scaling factor that accounts for the collection efficiency of our microscope setup, R is the reflection spectrum of the sample which is proportional to the density of photonic states, and $L\left(E,\tau_{dephase}\right)$ is the energy distribution of non-thermal carriers, which is approximated as a simple Lorentzian function, $f(E,T_l)$ and $f(E,T_e)$ is the Fermi-Dirac distribution of carriers thermalized at the lattice temperature, T_l, and the sub-population of hot carriers at the elevated temperature, T_e. The variable α is a free fit parameter that accounts for the relative size of the hot carrier population.[116] In our fitting routine, since the hot carrier population only contribute to anti-Stokes Raman signal at high wavenumber ($< -1000\ cm^{-1}$),[109] we can safely set α to 0 by neglecting anti-Stokes Raman signal at high wavenumber (Figure III.3b). Therefore, the remaining fitting parameters in this study are T_l, $\tau_{dephase}$, and D. This modifying fitting process is beneficial in terms of improving signal-to-noise ratio of Raman spectrum and fitting quality.

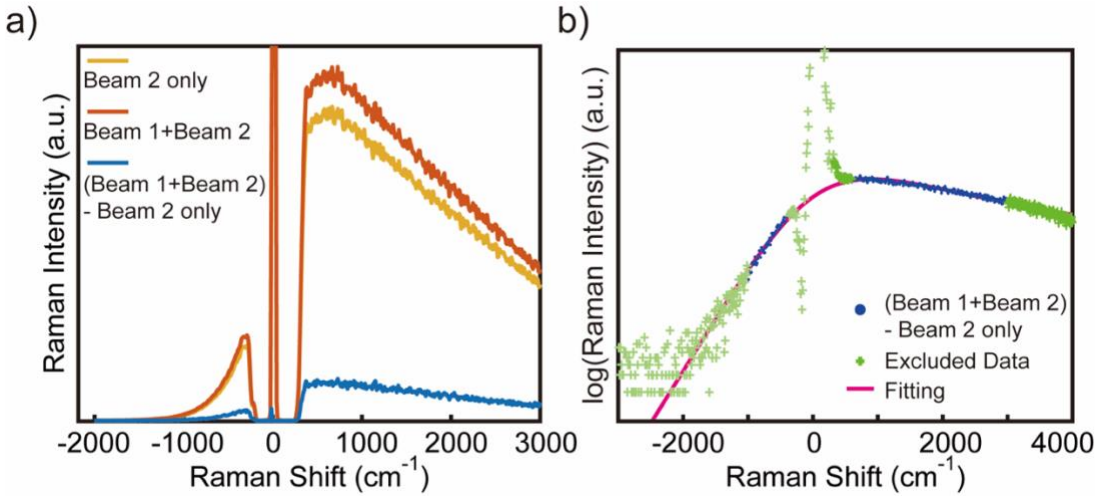

Figure III.3: (a) Raman spectra of both 532 nm Beam 1 and Beam 2 (red), Beam 2 only (yellow) and their difference which is used in the fitting routine (blue) (b) Compare experimental Raman spectra and fitting using Eq. 3.1. The green dots represent excluded data point due to Rayleigh scattering and neglecting hot electron contribution.

In order to extract Raman response of gold nanodisks array under different ellipticity excitation and get rid of polarization dependent instrument response, the dual-beam configuration was adopted (see section 3.4.2 for more details). Both Beam 1 and Beam 2 was 532 nm CW laser. Beam 1 was always linearly polarized and lower intensity, and its role was to probe electronic Raman response of the nanostructure. Beam 2 had higher intensity and its ellipticity was controlled by a pair of half waveplate and quarter waveplate, and its function was to generate photoheating in the nanostructure. To solely extract the Raman response from Beam 1, the Raman spectra of (Beam 1+ Beam 2) and (Beam 2 only) was measured, and the difference between the two can be regarded as the ellipticity excitation dependent Raman response of the gold nanodisks array (Figure

III.3a). The (Beam 1+ Beam 2) – (Beam 2 only) spectra was then fitted to Eq. 3.1 to extract T_l and $\tau_{dephase}$.

First, we examined the effect of total illumination intensity on the nanostructure temperature, T_l (Figure III.4a). Both Beam 1 and Beam 2 were linearly polarized in this case. A monotonic increase in T_l with total intensity was observed. This observation well matches with other reports studying on gold and copper nanostructures.[109, 114] The total intensity dependence can also serve as a calibration curve, which will be discussed in below.

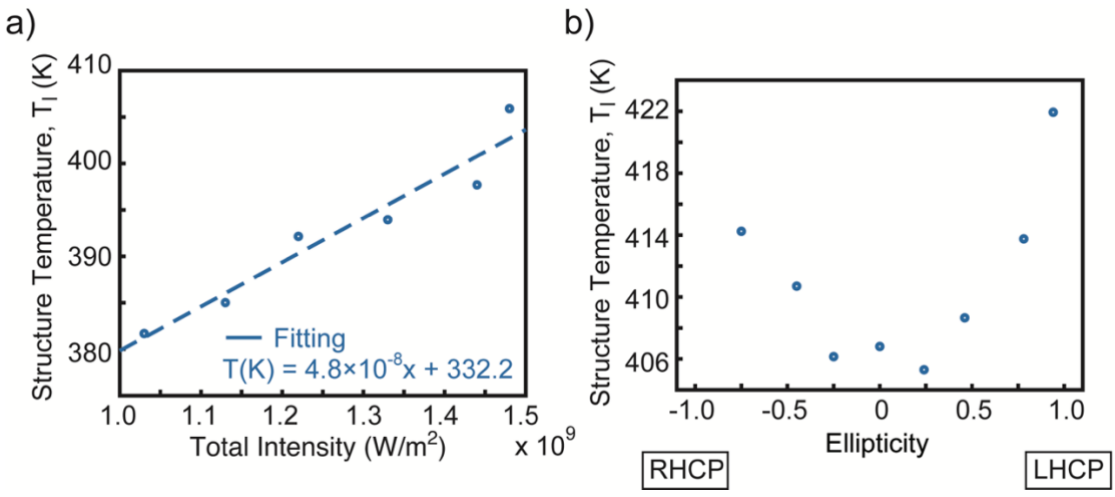

Figure III.4: (a) Temperature of gold nanodisks array as function of total intensity of Beam 1 and Beam 2. Both beams were linearly polarized. The intensity of Beam 1 was kept at 4.8×10^8 (W/m^2). The intensity of Beam 2 varied between 6.6 – 9.5×10^8 (W/m^2). (b) Temperature of gold nanodisks array as function of ellipticity of Beam 2. The intensity of Beam 1 was kept at 4.8×10^8 (W/m^2). The intensity of Beam 2 was kept at 9.5×10^8 (W/m^2). The slight asymmetry in ellipticity is due to the limitation of microscope system.

Next, we examined the effect of ellipticity of Beam 2 while the intensity of both beams was kept the same (Figure III.4b). For both RHCP and LHCP, T_l increases with increasing ellipticity. For the same ellipticity but opposite handedness, T_l increase was similar. Remind that our hypothesis is that the photothermal effect modulation is a result of electrical conductivity change in the nanostructure, which is due to the presence of circular current under circularly polarized excitation. This result well matches to our prediction because the magnitude of photothermal effect in enhanced with increasing ellipticity and is independent on helicity.[105] Moreover, $\tau_{dephase}$, which can also be extracted in our fitting routine, under linear and LHCP excitation was 19 and 23.9 fs, respectively. Since the σ is linear proportional to $\tau_{dephase}$, this observation is also in a good agreement qualitatively.

In Beam 2 ellipticity dependent experiment, the temperature difference between linear and LHCP is 15.1 K. Based on the total intensity dependent experiment (Figure III.4a), the nanostructure temperature increases 4.8 K for every 10^8 W/m^2 incident optical intensity. Thus, 15.1 K temperature increase means that, equivalently, the nanostructure experienced 3.1×10^8 W/m^2 more optical intensity under LHCP illumination. Since the total excitation intensity was kept at 1.4×10^9 W/m^2, we could conclude that the nanostructure absorbs 22% more, or equivalently, has 22% more absorption cross section under circularly polarized excitation. This increase can also be supported qualitatively by 26% increase in $\tau_{dephase}$ under LHCP illumination, since the absorption cross section and $\tau_{dephase}$ has a positive relation. A more detailed quantitative analysis will be performed in a short future to better support this statement.

Finally, we demonstrate that under externally applied magnetic field B_{app}, the degeneracy between RHCP and LHCP can be lifted. In this experiment, the ellipticity of Beam 2 was kept at 0 (linear), +0.67 (LHCP) and -0.67 (RHCP). An external magnetic field B_{app} = 0.2 T was applied parallel to the light propagation direction (Figure III.5a). T_l was measured as function of total intensity under different Beam 2 ellipticity. In Figure III.5b, with external magnetic field applied, T_l under LHCP excitation is higher than RHCP, while both of them is still higher than linear illumination. This phenomenon can be explained in the framework of the Drude model. Gu. *et al* have derived the equation of motion of free electron gas under circular polarization and external magnetic field, and the result showed that under week magnetic field, the magnitude of circular displacement current is affected by the coupling between metal and magnetic field, which in our case lead to change in conductivity.[31] This effect can also be considered in terms of the relative direction of M_{ind} and B_{app}. When M_{ind} and B_{app} are parallel, which is the case for LHCP, the effective resistance for circular electron motion is reduced, therefore the photothermal effect is enhanced due to more efficient Joule heating. Whereas the photothermal effect is suppressed if the M_{ind} and B_{app} are anti-parallel. While this measurement may lead us to determine the magnitude of M_{ind} in gold nanodisks array under CW illumination, further experiment is still needed to give a more accurate quantification.

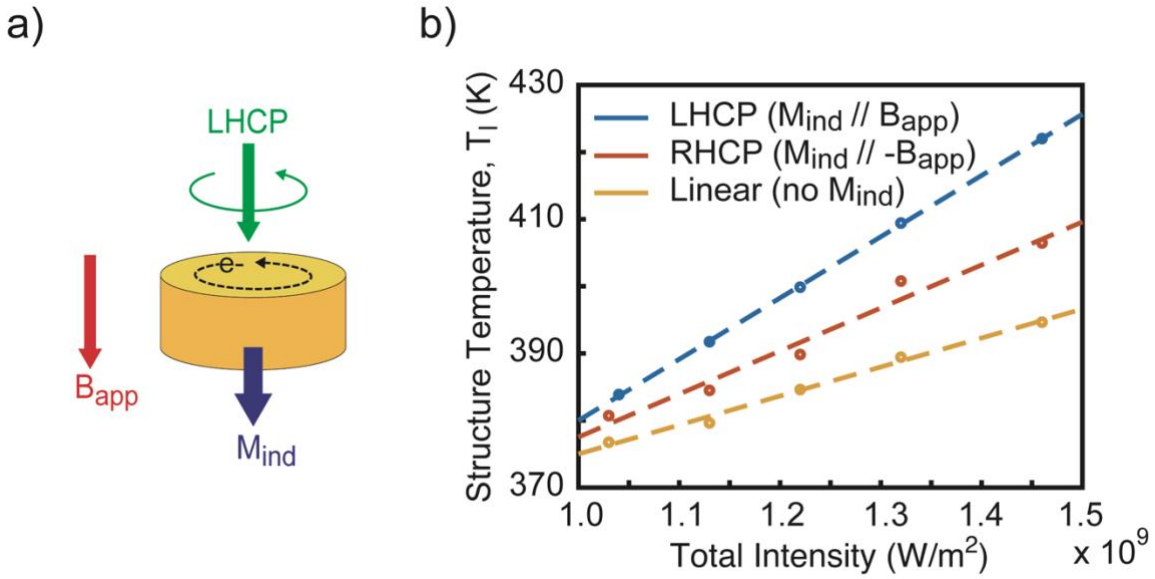

Figure III.5: (a) Illustration of the relation between incident light ellipticity, induced magnetization (M_{ind}) and external magnetic field (B_{app}). When incident light is LHCP, M_{ind} and B_{app} are parallel. (b) Temperature of gold nanodisks array as a function of total intensity under B_{app} = 0.2 Tesla and different ellipticity illumination. The fitting of each ellipticity: LHCP: $y = 9.1\times10^{8}\,x + 288.7$; RHCP: $y = 6.4\times10^{8}\,x + 313.4$; Linear: $y = 4.3\times10^{8}\,x + 311.8$.

3.3 Conclusion

This study provides a qualitative analysis to demonstrate the ability to modulate photothermal effect in plasmonic gold nanodisks array using light ellipticity. A dual-beam Raman spectroscopy successfully quantify the photothermal effect in nanostructures. The nanostructure temperature and plasmon dephasing time increase as light ellipticity increases, and regardless to the helicity. Our results support the hypothesis that anisotropic change in electrical conductivity under elliptical or circular polarization can result in Joule heating in nanostructures. Furthermore, under external magnetic field, the RHCP and LHCP result in different amount of photoheating due to suppress or enhancement of

circular displacement current. Our result provides a further insight of coherent interaction between conductive electrons and circularly polarized light, and also serve as another proof of existence of light-induced magnetic field in plasmonic nanostructures under CW excitation.

3.4 Experiment Detail

3.4.1 Nanostructure Fabrication

The gold nanodisks, with diameter d = 400 nm and pitch p = 700 nm, were fabricated on top of a 38 nm thick Al_2O_3 dielectric layer, which was sputtered on top of a perfectly reflecting 100 nm thick gold mirror. Prior to fabrication, a silicon substrate was cleaned using a combination of base piranha and UV-ozone. The 100 nm gold mirror was then thermally evaporated (Lesker PVD electron-beam evaporator) onto the silicon substrate. RF sputtering (Lesker PVD RF sputterer) was used to deposit the Al_2O_3 dielectric layer on top of the gold mirror. Next, 950 PMMA A4 was spin-coated onto the Al_2O_3 as the electron beam resist layer. Electron beam lithography (TESCAN MIRA3 EBL) was performed to pattern the 100 μm × 100 μm nanodisk array into the e-beam resist. After development, a 5 nm chrome adhesion layer was thermally deposited on the surface of the exposed PMMA, followed by a 100 nm layer of gold. Finally, liftoff was performed in acetone using a combination of pipet pumping and sonication, leaving only the nanodisk array on the surface of the substrate. The morphology of gold nanodisks array is confirmed by optical and SEM images (Figure III.6).

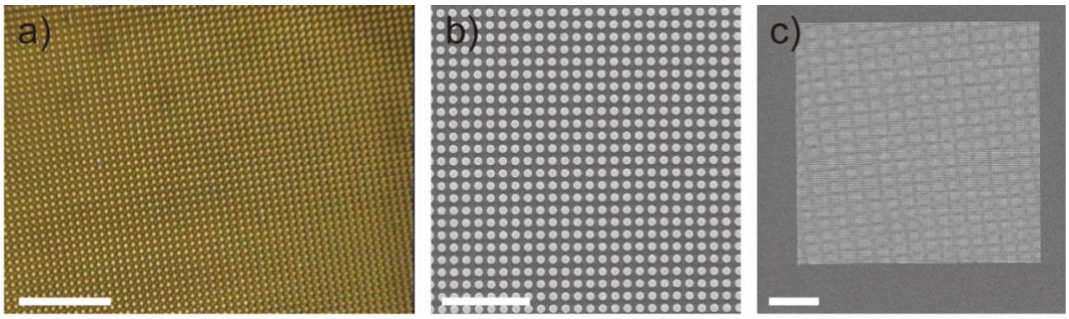

Figure III.6: (a) Optical and (b,c) SEM images of gold nanodisk array. Scale bar: 8 μm, 5 μm, 20 μm.

3.4.2 Dual-Beam Raman Spectroscopy

The scheme of the optical setup is shown in Figure III.7. Raman spectra was taken using a confocal microscope (Witec RA300) and spectrometer (UHTS300, grating = 300 g/mm). In dual-beam Raman spectroscopy experiment, Beam 1 was coupled through a fiber (Rayshield coupler, Witec). It was a 532 nm CW Nd:YAG laser with a spot size of 0.55 μm^2, always linearly polarized and lower intensity. Beam 2 was coupled through a free space coupler, and it was also a 532 CW laser with a spot size of 2 μm^2.

The ellipticity of beam 2 was controlled by a pair of half waveplate and quarter waveplate. The function of Beam 2 was to generate circular current in gold nanostructures and modulate photothermal effect. Both beams are focused by a 100× objective (Zeiss EC Epiplan Neofluar, NA = 0.9, WD = 0.31mm) on the gold nanostructures. The confocal microscope had alignment optimized to Beam 1, and excess scattering from Beam 2 was removed by a 532 NF, thus the effect of Beam 2 ellipticity on the instrument response can be neglected.

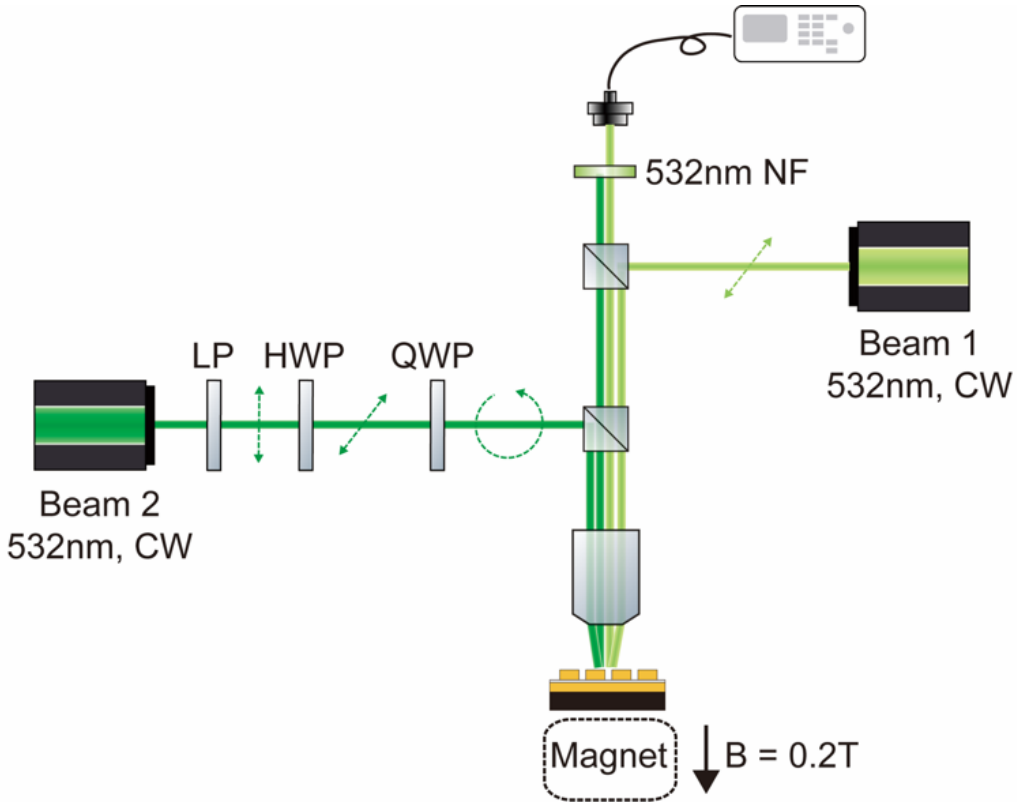

Figure III.7: Illustration of Dual-beam Raman spectroscopy setup. LP, Linear polarizer; HWP, Half wave plate; QWP, Quarter wave plate; NF, Notch filter.

CHAPTER IV

SIZE- AND TEMPERATURE-DEPENDENT PHOTOLUMINESCENCE SPECTRA OF STRONGLY CONFINED CESIUM LEAD BROMIDE QUANTUM DOTS[2]

4.1 Introduction

Lead halide perovskites (LHP) nanocrystals (NCs) have emerged as a strong contender for next-generation solid-state emitters[118-122] because of their high luminescence quantum yield,[67, 123-126] facile chemical bandgap tunability,[127, 128] and low-cost solution processability.[129, 130] Over the past few years, LHP-based light-emitting diodes (LEDs) have reached external quantum efficiencies > 20%, which is comparable to organic light-emitting diodes (OLEDs) and other colloidal semiconductor NCs used in commercialized displays.[54, 131] For photonic applications of semiconductor NCs, the spectral characteristics of the luminescence, i.e. energy and linewidth, is of great importance. Narrow emission bandwidth ensuring high color purity is desirable for display devices.[132, 133] On the other hand, broad or (and) multiple emission peaks covering a wider spectrum is more useful for lighting applications requiring white light.[134, 135]

So far, the majority of studies of the luminescence of LHP NCs and related optical properties have been focused on large NCs with weak or no quantum confinement. Therefore, the optical spectra of the NCs exhibit little size dependence. Tuning of the

[2] Reprint in part with permission from "Size- and temperature-dependent photoluminescence spectra of strongly confined $CsPbBr_3$ quantum dots" by Oscar Hsu-Cheng Cheng, Tian Qiao, Matthew Sheldon, Dong Hee Son. *Nanoscale*, **12**, 13113. Copyright 2020 by the Royal Society of Chemistry.

exciton luminescence spectrum was achieved mostly via chemical modification of the band, specifically by varying the halide composition and stoichiometry.[136, 137] Facile chemical exchange of halides (Cl, Br, and I) enables continuous tuning of the bandgap across the visible spectrum, and thus has been extensively explored as the means of controlling the luminescence color from LHP NCs. However, phase segregation or migration of halides under photoexcitation have been identified as potential issues for mixed-halide LHP NCs as the source of photons in technological applications.[138-142] More recently, synthetic methods for producing highly uniform LHP NCs with strong quantum confinement were developed.[143-147] Such quantum confinement can be used to vary the exciton transition energy as well as enhance the coupling of excitons to other degrees of freedom, further tuning optical and electronic properties similar to the extensively studied II-VI and IV-VI QDs.[148-151]

Either chemical tuning of the bandgap or size-dependent quantum confinement can vary the color of the emission from LHP NCs. However, these separate strategies do not have the same effect on all of the characteristics of the exciton luminescence. For instance, reducing the size of strongly confined NCs introduces size-dependent electron-hole interactions and vibronic coupling involving both lattice phonons and surface ligand.[152-154] Therefore, the energy and linewidth of exciton photoluminescence (PL) as well as the temperature dependence and exciton radiative lifetime can be quite different in comparison with non-confined mixed-halide LHP NCs exhibiting the same PL wavelength. Furthermore, the degree of ensemble size uniformity and the larger surface-to-volume ratio in strongly confined QDs can alter the characteristics of the exciton

luminescence significantly.[152] Therefore, it is important to understand the spectral characteristics of LHP QDs in the strongly confined regime to understand their potential utility as a source of photons.

Here, we measured the size- and temperature-dependent PL spectra of uniform ensembles of strongly confined $CsPbBr_3$ QDs and investigated the factors that dictate their spectral evolution when varying size and temperature. From the analysis of the temperature dependence of the PL spectral linewidth,[155-158] we obtained information about the effective strength of the coupling of excitons with the vibrational degrees of freedom as a function of the QD size. We also compared our results with those of CdSe QDs, an archetypal QD system with well-known size- and temperature-dependent PL, in order to highlight the unique aspects of the PL from strongly confined $CsPbBr_3$ QDs.

4.2 Result and Discussion

In this study, highly uniform ensembles of $CsPbBr_3$ QDs were prepared using the recently developed method that leverages thermodynamic equilibrium for the precise size control in strongly confined regime, which minimizes the effect of size dispersity on the PL spectra.[143] $CsPbBr_3$ QDs of varying sizes prepared in this study exhibit well-resolved confined exciton absorption and emission spectra as shown in Figure IV.1a. The edge length (d) of the QDs determined by transmission electron microscopy (TEM) images (Figure IV.1b-e) are in the range of 3.9 to 6.3 nm, which is smaller than twice the exciton Bohr radius of $CsPbBr_3$ ($2a_B$ = 7 nm).[159]

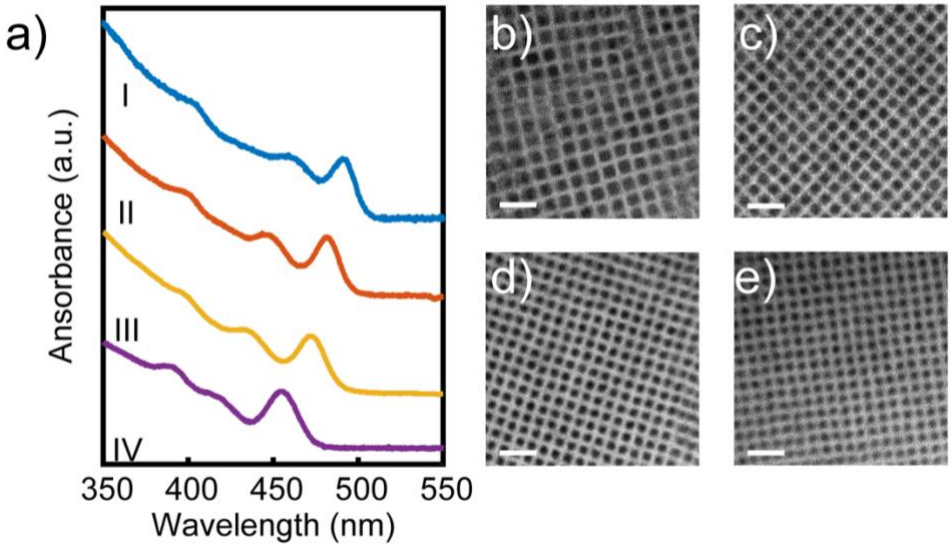

Figure IV.1: (a) Absorption spectra of different sizes of $CsPbBr_3$ QDs. (b-d) TEM images of $CsPbBr_3$ QDs. The average edge length of the QDs is (I) 6.3 nm, (II) 5.3 nm, (III) 4.7 nm, (IV) 3.9 nm. All scale bars are 20 nm.

For temperature-dependent PL measurements, the $CsPbBr_3$ QDs were deposited on a sapphire substrate by dipping the substrate into concentrated CsPbBr3 QD solutions dispersed in hexane, and then drying with nitrogen gas. The QD film prepared by this method is relatively close- packed with interparticle spacing of ~3 nm corresponding to the organic ligand on the surface of the QDs. Figure IV.2 compares the PL spectra of the colloidal solution of $CsPbBr_3$ QDs in hexane and the QD film deposited on a sapphire substrate. The PL spectra of $CsPbBr_3$ QDs in these different environments are nearly identical, while the film of the smallest QDs (d = 3.9 nm) exhibit a small blueshift compared to the solution of QDs. The similarity of the spectra from NCs in solution and deposited as films indicates a lack of interparticle electronic coupling. Other studies of $CsPbBr_3$ QD films often observe a redshift of the PL attributed to interparticle coupling.

The lack of interparticle coupling in this study is likely due to long ligands (oleylammonium bromide) passivating the surface of the QDs, separating them by ~3 nm as can be seen in the TEM images.

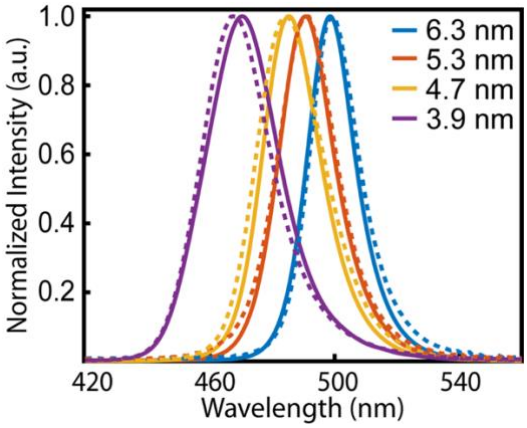

Figure IV.2: PL spectra of $CsPbBr_3$ QDs in hexane (solid line) and on sapphire substrate (dash line)

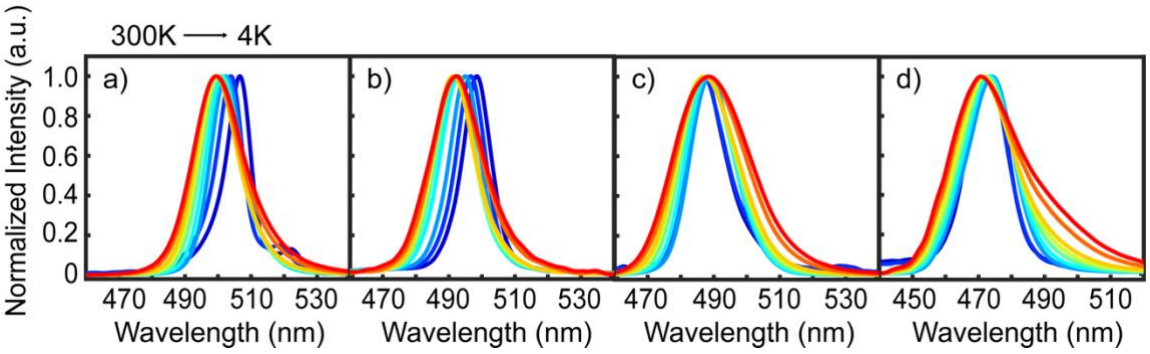

Figure IV.3: Normalized steady-state temperature dependent PL spectra of (a) 6.3 nm (b) 5.3 nm (c) 4.7 nm (d) 3.9 nm $CsPbBr_3$ QDs samples at temperatures between 4 and 300K.

Figure IV.3 shows the normalized temperature-dependent PL spectra of $CsPbBr_3$

QD films collected in the temperature range of 4 - 300K for four different sizes. The variation of the peak energy and linewidth with temperature and QD size were analyzed from these spectra. For more quantitative analysis of the PL peak energy and linewidth, the experimentally measured PL spectra were converted to the spectral line shape function on an energy axis, $S(E)$, through the Jacobian conversion, where the linewidth is directly proportional to the Franck-Condon factor.[160, 161] Both the peak energy and linewidth reported here were extracted from $S(E)$. The details of the conversion and analysis of the PL spectra are provided in the Appendix B.

Figure IV.4 shows the temperature-dependent PL peak energy, $E_{peak}(T)$ of $CsPbBr_3$ QDs of four different sizes. All four QDs show generally decreasing $E_{peak}(T)$ with decreases in temperature, which is similar to what has been observed in bulk and large non-confined NCs of $CsPbBr_3$.[155-158, 162] On the other hand, the smaller QDs show smaller shift of $E_{peak}(T)$ with temperature and also exhibit a bit more complex behavior above 200K, showing a small negative slope of $E_{peak}(T)$ with respect to T although its origin is not clear. Nevertheless, it is notable that the general redshift of $E_{peak}(T)$ with decreasing temperature in $CsPbBr_3$ QDs is opposite to the behavior of the majority of other semiconductor QDs (e.g. such CdSe) that exhibit blueshifts of the exciton absorption and PL peak with decreasing temperature. Furthermore, the slope (dE_{peak}/dT) is significantly smaller than in II-VI QDs of comparable size (-0.3 meV/K for CdSe QDs and -0.5 meV/K for CdS QDs).[163, 164] Below 200K, dE_{peak}/dT of $CsPbBr_3$ QDs is 0.05-0.18meV/K depending on the size, exhibiting much weaker dependence of E_{peak} on the temperature

(0.16, 0.18, 0.05, 0.11 meV for 6.3, 5.3, 4.7, 3.9 nm QDs). The general trend of $E_{peak}(T)$in LHP NCs can be explained by thermal expansion and exciton-phonon coupling. [165, 166] It has been shown that the bandgap decreases with decrease in lattice constant in LHP NCs.[165]

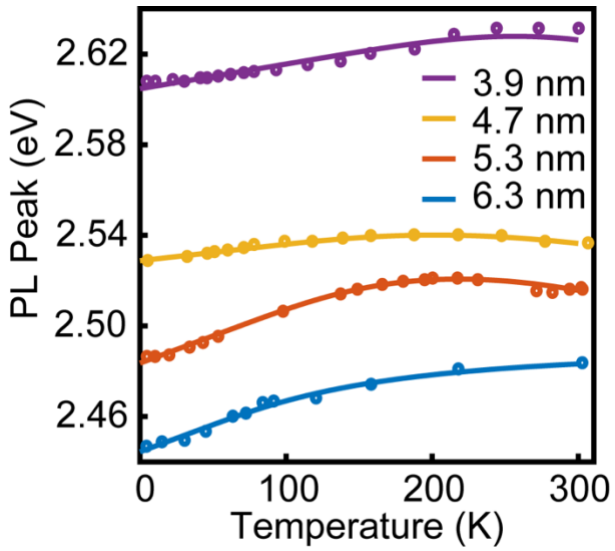

Figure IV.4: Temperature-dependent PL peak energy of different sizes of $CsPbBr_3$ QDs samples at temperatures between 4 and 300K.

The contribution of exciton-phonon coupling is estimated using a two-oscillator model, where acoustic and optical phonons contribute to the temperature dependent bandgap in opposite directions ($dE_{peak}/dT > 0$ for acoustic phonons, < 0 for optical phonons), thereby partially cancelling each other. Non-monotonous variation of $E_{peak}(T)$ in the smaller QDs (d = 5.3, 4.7, 3.9 nm) can therefore be interpreted as resulting from

variations in the balance between the two opposing contributions to the bandgap with the QD size.

Figure IV.5 shows the temperature-dependent full-width at half maximum (FWHM), $\Gamma(T)$, determined from the line shape, $S(E)$, of $CsPbBr_3$ QDs of four different sizes. We employ a linear exciton-phonon coupling model (Eq. 4.1) commonly used to analyze the temperature dependent $\Gamma(T)$ in order to extract the effective strength of coupling to phonons and the contribution from inhomogeneous broadening.[155, 165, 167-169]

$$\Gamma(T) = \gamma_{LO} N_{LO} + \gamma_{ac} T + \Gamma_{inh} \qquad (4.1)$$

In this model, $\Gamma(T)$ is expressed as the sum of three terms: temperature-independent inhomogeneous broadening (Γ_{inh}) and temperature-dependent optical ($\gamma_{LO} N_{LO}$) and acoustic ($\gamma_{ac} T$) phonon contributions. γ_{LO} represents coupling strength to longitudinal optical (LO) phonons, which is associated with number of the phonon mode, N_{LO}, described by the Bose-Einstein distribution, $N_{LO} = 1/\exp(E_{LO}/k_b T)$. Here, E_{LO} is the energy of the LO phonon and k_b is Boltzmann's constant. γ_{ac} represents coupling strength to acoustic phonons, and is mainly related to a deformation potential interaction in materials with cubic symmetry.[169]

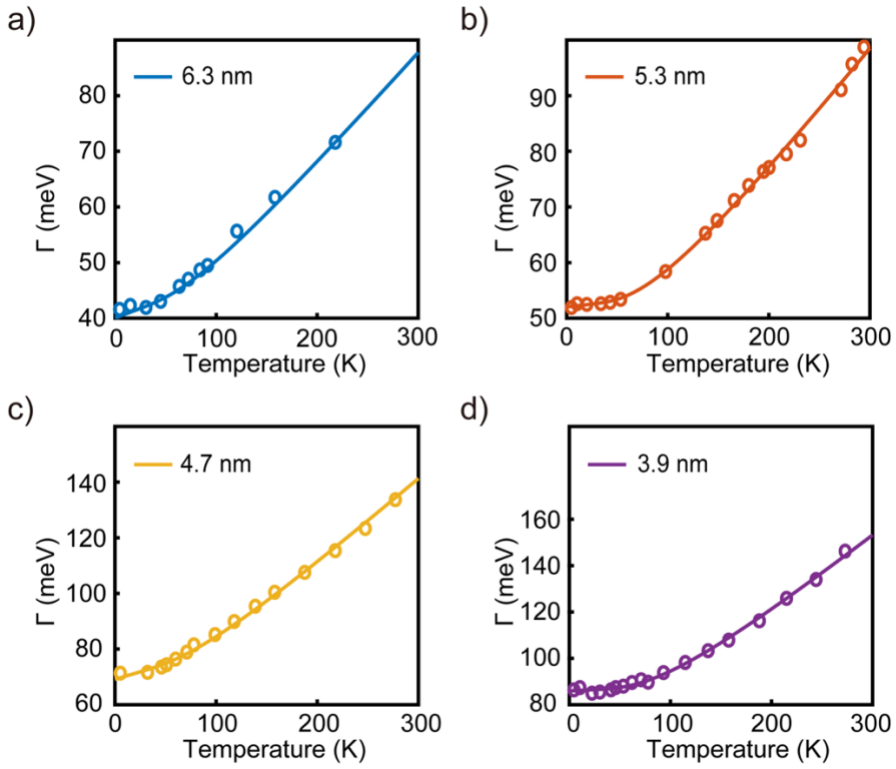

Figure IV.5: FWHM of the spectral lineshape as a function of temperature for (a) 6.3 nm (b) 5.3 nm (c) 4.7 nm (d) 3.9 nm QDs. The solid line are fits of Eq. 4.1.

	Size (nm)	γ_{LO} (meV)	γ_{ac} (μeV/K)	Γ_{inh} (meV)	E_{LO} (meV)
Sample I	6.3	32±13	70±75	40±2.5	20±9
Sample II	5.3	52±13	20±60	52±1.5	21±8
Sample III	4.7	52±18	20±70	69±3	22±11
Sample IV	3.9	89±27	22±50	86±2	23±6
B. Diroll *et al.*[155]	15	45	5	20	19
J. Ramade *et al.*‡ [167]	~7	42	8	0.4	16
F. Tang *et al.*[170]	Single crystal	11.61	10	9.02	20.01

Table IV.1: Extracted linewidth parameters. ‡ Single particle PL

Table IV.1 summarizes the parameters obtained by fitting the experimentally measured $\Gamma(T)$ to Eq. 4.1. Similar to other polar semiconductors, coupling to LO phonons ($\gamma_{LO}N_{LO}$) is the main contribution to the temperature-dependent broadening of the PL linewidth at high temperature (T > 100K). Since the contribution from the acoustic phonon ($\gamma_{ac}T$) accounts for < 10 % of the total temperature variation of $\Gamma(T)$, we will focus on coupling to LO phonon in our discussion of the size- and temperature-dependent $\Gamma(T)$. The value of E_{LO} obtained from the fit is near 20 meV for QDs of all sizes, and is close to E_{LO} of 19 meV measured from single macroscopic crystals of $CsPbBr_3$.[171] On the other hand, the coupling strength to LO phonons (γ_{LO}) shows a significant size dependence. γ_{LO} increases nearly 3 times (32 to 89 meV) as the size of the QD decreases from d = 6.3 to 3.9 nm. For comparison, γ_{LO} of weakly-confined $CsPbBr_3$ NCs from earlier studies are also added in Table IV.1, and these values are closer to that of the larger QDs in our study.[155, 167] This is an interesting contrast to CdSe QDs that show much smaller and more weakly size-dependent γ_{LO}, therefore exhibiting significantly weaker thermal broadening of PL linewidth and size dependence.[149, 152, 172] For instance, γ_{LO} of CdSe QDs calculated from the size-dependent Huang-Rhys factor increases very slowly from 10.9 meV to 12.6 meV as the QD size decreases from 5.23 nm to 2.56 nm.[172, 173] For a comparable size of QDs (d = ~3.9nm), $\Gamma(T)$ varies by more than twice as much in $CsPbBr_3$ than in CdSe (46 meV vs 20 meV), within the temperature range of 50-250K.[174] The stronger coupling of excitons with LO phonons in $CsPbBr_3$ QDs compared to CdSe QDs is not surprising, considering that lead halide perovskite materials are generally known to have larger exciton-phonon coupling.[155, 165] The strong exciton-phonon coupling in various inorganic

and hybrid lead halide perovskites manifests as facile formation of polarons, which has been shown in both calculations and experiments.[175-177] Strong exciton-phonon coupling was also considered to be responsible for the activation of parity-forbidden exciton transitions in strongly confined $CsPbBr_3$ QDs, whereby polaron formation lifted the optical selection rule.[178] This strong size-dependence of γ_{LO} in $CsPbBr_3$ QDs is quite intriguing, considering that typical semiconductor QDs such as CdSe QDs exhibit weak size dependence. Earlier studies in various semiconductor QDs showed evidence that increasing the coupling of vibrational modes with surfaces and surface ligands by decreasing size results in the larger effective coupling strength between excitons and vibrational degrees of freedom. For instance, $\Gamma(T)/T$ in 2 nm CdSe QDs increased by 2.2 times by changing the ligand from dodecanethiol to tetradecylphosphonic acid, while such sensitivity to the ligand is absent in much larger QDs.[152] In the case of monolayer WSe_2 and WS_2 QDs, a large increase of $\Gamma(T)$ of the PL at room temperature and Stokes shift was explained by increased coupling of excitons to the chemical bonds at edges with decreasing size.[179, 180] Since the model described in Eq. 4.1 does not specifically include the terms representing the coupling of excitons to surface-specific modes, γ_{LO} determined from the fitting represent the combined effect of coupling to both lattice LO phonon mode and local vibrational modes at surface, such as the bond from ligands. This suggests that the strong dependence of γ_{LO} on the size of $CsPbBr_3$ QDs reflect the stronger influence of the surface in coupling with exciton compared to CdSe QDs. At cryogenic temperatures, Γ_{inh} is still relatively large compared to the estimated linewidth broadening based on the QD size distribution determined from the analysis of TEM images (±5 % at FWHM) and

the experimentally determined size-dependent bandgap.[143] The inhomogeneous linewidth purely from the size distribution is estimated to be < 35 meV for the QDs with average size of 4.7 nm. Much larger Γ_{inh} of 69 meV indicates that the inhomogeneous broadening of the PL observed in $CsPbBr_3$ QDs has contribution from not only the size distribution but also from other contributions. While the exact nature of such additional contribution is not clear yet, variations of the surface ligand density or local fluctuation of charges within the film may have contributed to the inhomogeneous broadening.

4.3 Conclusion

In summary, the PL spectra of strongly quantum confined $CsPbBr_3$ QDs were measured as a function of size and temperature in order to investigate the factors that determine the spectral evolution with temperature and the degree of quantum confinement. The peak energy of the PL shows much weaker dependence on the temperature for all QD sizes compared to the other well-known semiconductor QDs such as II-VI QDs. On the other hand, the PL linewidth exhibits stronger dependence on both the size of the QD and temperature compared to II-VI QDs, indicating stronger exciton-phonon coupling. γ_{LO} determined from spectral linewidth analysis is several times larger than that of CdSe QDs for comparable sizes, consistent with generally stronger exciton-coupling known for various metal halide perovskite materials in the bulk phase. The size dependence of γ_{LO} is also much stronger than CdSe QDs, indicating the stronger influence of the surface vibrational degrees of freedom for the overall effective exciton-phonon coupling. This detailed information about the dependence of PL spectra on size and temperature will be

valuable in applications that employ strongly quantum-confined metal halide perovskite QDs as a source of photons.

4.4 Experiment Detail

4.4.1 Sample Preparation

Size-controlled $CsPbBr_3$ QDs were synthesized via the hot-injection method reported by Dong *et al*.[70] The synthesized QDs were purified using ethyl acetate to remove all remaining unreacted precursors and excess ligands by centrifuging the solution at 3500 rpm at 5 min. The precipitate was recovered and redispersed in hexane for all spectroscopic measurements in solution sample and preparation of QD film on a sapphire substrate.

4.4.2 Temperature-dependent PL measurement

Temperature-dependent PL measurements were made using an open-cycle cryostat (ST-100, Janis) using liquid nitrogen and liquid helium as the cryogen. The QD film on sapphire substrate was excited at 405 nm using a CW diode laser (RGBLase, FBB-405-200-FM-E-1-0). The excitation power was kept below ~1 mW with a 3 mm beam diameter to avoid heating of the substrate. The PL spectra were recorded with two different CCD spectrometers (QE65000, Ocean Optics and WiTec alpha 300), which give identical line shape after the calibration of the spectral response of each spectrometer. A 405 nm notch filter was used to block the excitation light in PL spectrum measurement and its transmission spectrum was accounted for in the analysis of the PL spectra.

CHAPTER V

SUMMARY AND OUTLOOK

Circularly polarized illumination generates static magnetic field as well as coherent circular current in plasmonic gold nanostructures. Effective light-induced magnetic field as large as 38 mT was observed by using time-resolved pump-probe Faraday rotation spectroscopy. The magnetization dynamics was instantaneous to the excitation pulse due to its orbital angular momentum nature, in stark contrast to common ferromagnetic materials where the magnetic response is a result of electron spin angular momentum. Though our study only focused on gold nanoparticles, the effect should be generic to all plasmonic systems. With proper design of plasmonic nanostructure geometry or combination with ferromagnetic materials, ultrafast and localized control of magnetism could be realized in the short future.

Furthermore, in Chapter III, anisotropic modulation of electrical conductivity and plasmon dephasing time was monitored by photothermal effect in gold nanodisks array. Pronounced structure temperature and plasmon dephasing time modulation was observed under different ellipticity illumination, regardless to the helicity. With external magnetic field applied, the photothermal effect was enhanced (suppressed) if light-induced magnetization and external magnetic field were parallel (anti-parallel). While more detailed calibration and calculation will be required to draw quantitative conclusions, this preliminary result demonstrated a possibility to modulate fundamental optical properties

with light ellipticity, shading light on potential application in photocatalysis and localized photothermal control in nanometer scale.

Finally, the photoluminescence energy and linewidth of strongly quantum confined $CsPbBr_3$ QDs was explored. The size and temperature dependence were found significantly different from other common semiconducting nanocrystals system, owing to strong coupling strength to longitudinal optical phonon. Proper engineering of the surface ligands and embedded environment will be of interest for solid-state lightening community, due to their remarkable effect on the photoluminescence linewidth as well.

REFERENCES

1. Hartland, G. V., Optical studies of dynamics in noble metal nanostructures. *Chem Rev* **2011,** *111* (6), 3858-87.

2. Kravets, V. G.; Kabashin, A. V.; Barnes, W. L.; Grigorenko, A. N., Plasmonic Surface Lattice Resonances: A Review of Properties and Applications. *Chemical Reviews* **2018,** *118* (12), 5912-5951.

3. Li, Y., *Plasmonic Optics: Theory and Applications*. SPIE Press: 2017.

4. Rangel, T.; Kecik, D.; Trevisanutto, P. E.; Rignanese, G. M.; Van Swygenhoven, H.; Olevano, V., Band structure of gold from many-body perturbation theory. *Physical Review B* **2012,** *86* (12), 125125.

5. Baida, H.; Mongin, D.; Christofilos, D.; Bachelier, G.; Crut, A.; Maioli, P.; Del Fatti, N.; Vallée, F., Ultrafast Nonlinear Optical Response of a Single Gold Nanorod near Its Surface Plasmon Resonance. *Physical Review Letters* **2011,** *107* (5), 057402.

6. Tian, Y.; Tatsuma, T., Mechanisms and Applications of Plasmon-Induced Charge Separation at TiO_2 Films Loaded with Gold Nanoparticles. *Journal of the American Chemical Society* **2005,** *127* (20), 7632-7637.

7. Anker, J. N.; Hall, W. P.; Lyandres, O.; Shah, N. C.; Zhao, J.; Van Duyne, R. P., Biosensing with plasmonic nanosensors. *Nature Materials* **2008,** *7* (6), 442-453.

8. Oshikiri, T.; Ueno, K.; Misawa, H., Plasmon-Induced Ammonia Synthesis through Nitrogen Photofixation with Visible Light Irradiation. *Angewandte Chemie International Edition* **2014,** *53* (37), 9802-9805.

9. Heilweil, E. J.; Hochstrasser, R. M., Nonlinear spectroscopy and picosecond transient grating study of colloidal gold. *The Journal of Chemical Physics* **1985,** *82* (11), 4762-4770.

10. Therrien, A. J.; Kale, M. J.; Yuan, L.; Zhang, C.; Halas, N. J.; Christopher, P., Impact of chemical interface damping on surface plasmon dephasing. *Faraday Discussions* **2019,** *214* (0), 59-72.

11. Bosman, M.; Zhang, L.; Duan, H.; Tan, S. F.; Nijhuis, C. A.; Qiu, C. W.; Yang, J. K. W., Encapsulated Annealing: Enhancing the Plasmon Quality Factor in Lithographically–Defined Nanostructures. *Scientific Reports* **2014,** *4* (1), 5537.

12. Zhang, F.; Proust, J.; Gérard, D.; Plain, J.; Martin, J., Reduction of Plasmon Damping in Aluminum Nanoparticles with Rapid Thermal Annealing. *The Journal of Physical Chemistry C* **2017,** *121* (13), 7429-7434.

13. Ueno, K.; Yang, J.; Sun, Q.; Aoyo, D.; Yu, H.; Oshikiri, T.; Kubo, A.; Matsuo, Y.; Gong, Q.; Misawa, H., Control of plasmon dephasing time using stacked nanogap gold structures for strong near-field enhancement. *Applied Materials Today* **2019,** *14*, 159-165.

14. Brandstetter-Kunc, A.; Weick, G.; Weinmann, D.; Jalabert, R. A., Decay of dark and bright plasmonic modes in a metallic nanoparticle dimer. *Physical Review B* **2015,** *91* (3), 035431.

15. Yang, J.; Sun, Q.; Ueno, K.; Shi, X.; Oshikiri, T.; Misawa, H.; Gong, Q., Manipulation of the dephasing time by strong coupling between localized and propagating surface plasmon modes. *Nature Communications* **2018,** *9* (1), 4858.

16. Márquez, A.; Esquivel-Sirvent, R., Terahertz response of plasmonic nanoparticles: Plasmonic Zeeman Effect. *Opt. Express* **2020,** *28* (26), 39005-39016.

17. Pineider, F.; Campo, G.; Bonanni, V.; Fernandez Cde, J.; Mattei, G.; Caneschi, A.; Gatteschi, D.; Sangregorio, C., Circular magnetoplasmonic modes in gold nanoparticles. *Nano Lett* **2013,** *13* (10), 4785-9.

18. Weick, G.; Weinmann, D., Lifetime of the surface magnetoplasmons in metallic nanoparticles. *Physical Review B* **2011,** *83* (12), 125405.

19. Scott, G. B.; Lacklison, D. E.; Ralph, H. I.; Page, J. L., Magnetic circular dichroism and Faraday rotation spectra of $Y_3Fe_5O_{12}$. *Physical Review B* **1975,** *12* (7), 2562-2571.

20. Andlauer, B.; Schneider, J.; Wettling, W., Optical and magneto-optical properties of YIG and $FeBO_3$. *Applied physics* **1976,** *10* (3), 189-201.

21. Bennett, H. S.; Stern, E. A., Faraday Effect in Solids. *Physical Review* **1965,** *137* (2A), A448-A461.

22. Stern, E. A.; McGroddy, J. C.; Harte, W. E., Polar Reflection Faraday Effect in Metals. *Physical Review* **1964,** *135* (5A), A1306-A1314.

23. McGroddy, J. C.; McAlister, A. J.; Stern, E. A., Polar Reflection Faraday Effect in Silver and Gold. *Physical Review* **1965,** *139* (6A), A1844-A1848.

24. Scott, G.; Lacklison, D., Magnetooptic properties and applications of bismuth substituted iron garnets. *IEEE Transactions on Magnetics* **1976,** *12* (4), 292-311.

25. Bossini, D.; Belotelov, V. I.; Zvezdin, A. K.; Kalish, A. N.; Kimel, A. V., Magnetoplasmonics and Femtosecond Optomagnetism at the Nanoscale. *ACS Photonics* **2016,** *3* (8), 1385-1400.

26. Haider, T., A Review of Magneto-Optic Effects and Its Application. *International Journal of Electromagnetics and Applications* **2017,** *7* (1), 8.

27. Hui, P. M.; Stroud, D., Theory of Faraday rotation by dilute suspensions of small particles. *Applied Physics Letters* **1987,** *50* (15), 950-952.

28. Jain, P. K.; Xiao, Y.; Walsworth, R.; Cohen, A. E., Surface Plasmon Resonance Enhanced Magneto-Optics (SuPREMO)- Faraday Rotation Enhancement in Gold-Coated Iron Oxide Nanocrystals.pdf. *Nano Letters* **2009,** *9* (4).

29. Dani, R. K.; Wang, H.; Bossmann, S. H.; Wysin, G.; Chikan, V., Faraday rotation enhancement of gold coated Fe_2O_3 nanoparticles: comparison of experiment and theory. *J Chem Phys* **2011,** *135* (22), 224502.

30. Gevorkian, Z.; Gasparian, V., Plasmon-enhanced Faraday rotation in thin films. *Physical Review A* **2014,** *89* (2), 023830.

31. Gu, Y.; Kornev, K. G., Plasmon enhanced direct and IFE in nonmagnetic nanocomposites. *J. Opt. Soc. Am. B* **2010,** *27* (11).

32. Cheng, O. H.-C.; Son, D. H.; Sheldon, M., Light-induced magnetism in plasmonic gold nanoparticles. *Nature Photonics* **2020,** *14* (6), 365-368.

33. Chin, J. Y.; Steinle, T.; Wehlus, T.; Dregely, D.; Weiss, T.; Belotelov, V. I.; Stritzker, B.; Giessen, H., Nonreciprocal plasmonics enables giant enhancement of thin-film Faraday rotation. *Nat Commun* **2013,** *4*, 1599.

34. Gu, Y.; Kornev, K. G., Plasmon enhanced direct and inverse Faraday effects in non-magnetic nanocomposites. *Journal of the Optical Society of America B* **2010,** *27* (11), 2165-2173.

35. van der Ziel, J. P.; Pershan, P. S.; Malmstrom, L. D., Optically-Induced Magnetization Resulting from the Inverse Faraday Effect. *Physical Review Letters* **1965,** *15* (5), 190-193.

36. Mikhaylovskiy, R. V.; Hendry, E.; Kruglyak, V. V., Ultrafast inverse Faraday effect in a paramagnetic terbium gallium garnet crystal. *Physical Review B* **2012,** *86* (10).

37. Raja, M. Y. A.; Allen, D.; Sisk, W., Room-temperature inverse Faraday effect in terbium gallium garnet. *Applied Physics Letters* **1995,** *67* (15), 2123-2125.

38. Belotelov, V. I.; Bezus, E. A.; Doskolovich, L. L.; Kalish, A. N.; Zvezdin, A. K., Inverse Faraday effect in plasmonic heterostructures. *Journal of Physics: Conference Series* **2010,** *200* (9).

39. Monticone, F.; Alù, A., The quest for optical magnetism: from split-ring resonators to plasmonic nanoparticles and nanoclusters. *J. Mater. Chem. C* **2014,** *2* (43), 9059-9072.

40. Kirilyuk, A.; Kimel, A. V.; Rasing, T., Ultrafast optical manipulation of magnetic order. *Reviews of Modern Physics* **2010,** *82* (3), 2731-2784.

41. Hertel, R., Theory of the inverse Faraday effect in metals. *Journal of Magnetism and Magnetic Materials* **2006,** *303* (1), L1-L4.

42. Hertel, R.; Fähnle, M., Macroscopic drift current in the inverse Faraday effect. *Physical Review B* **2015,** *91* (2).

43. Nadarajah, A.; Sheldon, M. T., Optoelectronic phenomena in gold metal nanostructures due to the inverse Faraday effect. *Opt Express* **2017,** *25* (11), 12753-12764.

44. Karakhanyan, V.; Lefier, Y.; Eustache, C.; Grosjean, T., Optomagnets in nonmagnetic plasmonic nanostructures. *Opt. Lett.* **2021,** *46* (3), 613-616.

45. Berritta, M.; Mondal, R.; Carva, K.; Oppeneer, P. M., Ab Initio Theory of Coherent Laser-Induced Magnetization in Metals. *Phys Rev Lett* **2016,** *117* (13), 137203.

46. Hurst, J.; Oppeneer, P. M.; Manfredi, G.; Hervieux, P.-A., Magnetic moment generation in small gold nanoparticles via the plasmonic inverse Faraday effect. *Physical Review B* **2018,** *98* (13), 134439.

47. Sinha-Roy, R.; Hurst, J.; Manfredi, G.; Hervieux, P.-A., Driving Orbital Magnetism in Metallic Nanoparticles through Circularly Polarized Light: A Real-Time TDDFT Study. *ACS Photonics* **2020,** *7* (9), 2429-2439.

48. Green, M. A.; Ho-Baillie, A.; Snaith, H. J., The emergence of perovskite solar cells. *Nature Photonics* **2014,** *8* (7), 506-514.

49. A decade of perovskite photovoltaics. *Nature Energy* **2019,** *4* (1), 1-1.

50. Laboratory, N. R. E. Best Research-Cell Efficiency Chart. https://www.nrel.gov/pv/cell-efficiency.html (accessed Feb. 05, 2021).

51. Huang, J.; Yuan, Y.; Shao, Y.; Yan, Y., Understanding the physical properties of hybrid perovskites for photovoltaic applications. *Nature Reviews Materials* **2017,** *2* (7), 17042.

52. Park, N.-G., Perovskite solar cells: an emerging photovoltaic technology. *Materials Today* **2015,** *18* (2), 65-72.

53. Zhu, X. Y.; Podzorov, V., Charge Carriers in Hybrid Organic-Inorganic Lead Halide Perovskites Might Be Protected as Large Polarons. *J Phys Chem Lett* **2015,** *6* (23), 4758-61.

54. Lin, K.; Xing, J.; Quan, L. N.; de Arquer, F. P. G.; Gong, X.; Lu, J.; Xie, L.; Zhao, W.; Zhang, D.; Yan, C.; Li, W.; Liu, X.; Lu, Y.; Kirman, J.; Sargent, E. H.; Xiong, Q.; Wei, Z., Perovskite light-emitting diodes with external quantum efficiency exceeding 20 per cent. *Nature* **2018,** *562* (7726), 245-248.

55. Zhang, L.; Yang, X.; Jiang, Q.; Wang, P.; Yin, Z.; Zhang, X.; Tan, H.; Yang, Y.; Wei, M.; Sutherland, B. R.; Sargent, E. H.; You, J., Ultra-bright and highly efficient inorganic based perovskite light-emitting diodes. *Nature Communications* **2017,** *8* (1), 15640.

56. Xing, G.; Mathews, N.; Lim, S. S.; Yantara, N.; Liu, X.; Sabba, D.; Gratzel, M.; Mhaisalkar, S.; Sum, T. C., Low-temperature solution-processed wavelength-tunable perovskites for lasing. *Nat Mater* **2014,** *13* (5), 476-80.

57. Brenner, P.; Bar-On, O.; Jakoby, M.; Allegro, I.; Richards, B. S.; Paetzold, U. W.; Howard, I. A.; Scheuer, J.; Lemmer, U., Continuous wave amplified spontaneous emission in phase-stable lead halide perovskites. *Nat Commun* **2019,** *10* (1), 988.

58. Kang, J.; Wang, L. W., High Defect Tolerance in Lead Halide Perovskite $CsPbBr_3$. *J Phys Chem Lett* **2017,** *8* (2), 489-493.

59. Yuan, G.; Ritchie, C.; Ritter, M.; Murphy, S.; Gómez, D. E.; Mulvaney, P., The Degradation and Blinking of Single $CsPbI_3$ Perovskite Quantum Dots. *The Journal of Physical Chemistry C* **2018,** *122* (25), 13407-13415.

60. Liu, L.; Deng, L.; Huang, S.; Zhang, P.; Linnros, J.; Zhong, H.; Sychugov, I., Photodegradation of Organometal Hybrid Perovskite Nanocrystals: Clarifying the Role of Oxygen by Single-Dot Photoluminescence. *J Phys Chem Lett* **2019,** *10* (4), 864-869.

61. Lorenzon, M.; Sortino, L.; Akkerman, Q.; Accornero, S.; Pedrini, J.; Prato, M.; Pinchetti, V.; Meinardi, F.; Manna, L.; Brovelli, S., Role of Nonradiative Defects and Environmental Oxygen on Exciton Recombination Processes in $CsPbBr_3$ Perovskite Nanocrystals. *Nano Letters* **2017,** *17* (6), 3844-3853.

62. Limmer, D. T.; Ginsberg, N. S., Photoinduced phase separation in the lead halides is a polaronic effect. *The Journal of Chemical Physics* **2020,** *152* (23), 230901.

63. Mao, W.; Hall, C. R.; Bernardi, S.; Cheng, Y.-B.; Widmer-Cooper, A.; Smith, T. A.; Bach, U., Light-induced reversal of ion segregation in mixed-halide perovskites. *Nature Materials* **2021,** *20* (1), 55-61.

64. Zhao, L.; Roh, K.; Kacmoli, S.; Al Kurdi, K.; Jhulki, S.; Barlow, S.; Marder, S. R.; Gmachl, C.; Rand, B. P., Thermal Management Enables Bright and Stable Perovskite Light-Emitting Diodes. *Advanced Materials* **2020,** *32* (25), 2000752.

65. Zou, W.; Li, R.; Zhang, S.; Liu, Y.; Wang, N.; Cao, Y.; Miao, Y.; Xu, M.; Guo, Q.; Di, D.; Zhang, L.; Yi, C.; Gao, F.; Friend, R. H.; Wang, J.; Huang, W., Minimising efficiency roll-off in high-brightness perovskite light-emitting diodes. *Nature Communications* **2018,** *9* (1), 608.

66. Protesescu, L.; Yakunin, S.; Bodnarchuk, M. I.; Krieg, F.; Caputo, R.; Hendon, C. H.; Yang, R. X.; Walsh, A.; Kovalenko, M. V., Nanocrystals of Cesium Lead Halide Perovskites (CsPbX(3), X = Cl, Br, and I): Novel Optoelectronic Materials Showing Bright Emission with Wide Color Gamut. *Nano Lett* **2015,** *15* (6), 3692-6.

67. Koscher, B. A.; Swabeck, J. K.; Bronstein, N. D.; Alivisatos, A. P., Essentially Trap-Free $CsPbBr_3$ Colloidal Nanocrystals by Postsynthetic Thiocyanate Surface Treatment. *Journal of the American Chemical Society* **2017,** *139* (19), 6566-6569.

68. Zhang, B.; Goldoni, L.; Lambruschini, C.; Moni, L.; Imran, M.; Pianetti, A.; Pinchetti, V.; Brovelli, S.; De Trizio, L.; Manna, L., Stable and Size Tunable $CsPbBr_3$ Nanocrystals Synthesized with Oleylphosphonic Acid. *Nano Letters* **2020,** *20* (12), 8847-8853.

69. Shynkarenko, Y.; Bodnarchuk, M. I.; Bernasconi, C.; Berezovska, Y.; Verteletskyi, V.; Ochsenbein, S. T.; Kovalenko, M. V., Direct Synthesis of Quaternary Alkylammonium-Capped Perovskite Nanocrystals for Efficient Blue and Green Light-Emitting Diodes. *ACS Energy Letters* **2019,** *4* (11), 2703-2711.

70. Dong, Y.; Qiao, T.; Kim, D.; Parobek, D.; Rossi, D.; Son, D. H., Precise Control of Quantum Confinement in Cesium Lead Halide Perovskite Quantum Dots via Thermodynamic Equilibrium. *Nano Lett* **2018,** *18* (6), 3716-3722.

71. Castañeda, J. A.; Nagamine, G.; Yassitepe, E.; Bonato, L. G.; Voznyy, O.; Hoogland, S.; Nogueira, A. F.; Sargent, E. H.; Cruz, C. H. B.; Padilha, L. A., Efficient Biexciton Interaction in Perovskite Quantum Dots Under Weak and Strong Confinement. *ACS Nano* **2016,** *10* (9), 8603-8609.

72. Hens, Z.; Moreels, I., Light absorption by colloidal semiconductor quantum dots. *Journal of Materials Chemistry* **2012,** *22* (21).

73. Puthenpurayil, J.; Cheng, O. H.-C.; Qiao, T.; Rossi, D.; Son, D. H., On the determination of absorption cross section of colloidal lead halide perovskite quantum dots. *The Journal of Chemical Physics* **2019,** *151* (15), 154706.

74. Becker, M. A.; Vaxenburg, R.; Nedelcu, G.; Sercel, P. C.; Shabaev, A.; Mehl, M. J.; Michopoulos, J. G.; Lambrakos, S. G.; Bernstein, N.; Lyons, J. L.; Stoferle, T.; Mahrt, R. F.; Kovalenko, M. V.; Norris, D. J.; Raino, G.; Efros, A. L., Bright triplet excitons in caesium lead halide perovskites. *Nature* **2018,** *553* (7687), 189-193.

75. Tamarat, P.; Bodnarchuk, M. I.; Trebbia, J. B.; Erni, R.; Kovalenko, M. V.; Even, J.; Lounis, B., The ground exciton state of formamidinium lead bromide perovskite nanocrystals is a singlet dark state. *Nat Mater* **2019,** *18* (7), 717-724.

76. Sercel, P. C.; Lyons, J. L.; Wickramaratne, D.; Vaxenburg, R.; Bernstein, N.; Efros, A. L., Exciton Fine Structure in Perovskite Nanocrystals. *Nano Lett* **2019,** *19* (6), 4068-4077.

77. Rossi, D.; Qiao, T.; Liu, X.; Khurana, M.; Akimov, A. V.; Cheon, J.; Son, D. H., Size-dependent dark exciton properties in cesium lead halide perovskite quantum dots. *The Journal of Chemical Physics* **2020,** *153* (18), 184703.

78. Rossi, D.; Liu, X.; Lee, Y.; Khurana, M.; Puthenpurayil, J.; Kim, K.; Akimov, A. V.; Cheon, J.; Son, D. H., Intense Dark Exciton Emission from Strongly Quantum-Confined $CsPbBr_3$ Nanocrystals. *Nano Letters* **2020,** *20* (10), 7321-7326.

79. Qiao, T.; Son, D. H., Synthesis and Properties of Strongly Quantum-Confined Cesium Lead Halide Perovskite Nanocrystals. *Accounts of Chemical Research* **2021**.

80. Tang, X.; Yang, J.; Li, S.; Chen, W.; Hu, Z.; Qiu, J., $CsPbBr_3$/CdS Core/Shell Structure Quantum Dots for Inverted Light-Emitting Diodes Application. *Frontiers in Chemistry* **2019,** *7* (499).

81. Wang, X.; Bao, Z.; Chang, Y.-C.; Liu, R.-S., Perovskite Quantum Dots for Application in High Color Gamut Backlighting Display of Light-Emitting Diodes. *ACS Energy Letters* **2020,** *5* (11), 3374-3396.

82. Zhang, Q.; Shang, Q.; Su, R.; Do, T. T. H.; Xiong, Q., Halide Perovskite Semiconductor Lasers: Materials, Cavity Design, and Low Threshold. *Nano Letters* **2021**.

83. Stanciu, C. D.; Hansteen, F.; Kimel, A. V.; Kirilyuk, A.; Tsukamoto, A.; Itoh, A.; Rasing, T., All-optical magnetic recording with circularly polarized light. *Phys Rev Lett* **2007,** *99* (4), 047601.

84. Wolf, S. A.; Awschalom, D. D.; Buhrman, R. A.; Daughton, J. M.; von Molnár, S.; Roukes, M. L.; Chtchelkanova, A. Y.; Treger, D. M., Spintronics: A Spin-Based Electronics Vision for the Future. *Science* **2001,** *294* (5546), 1488.

85. Chai, Z.; Hu, X.; Wang, F.; Niu, X.; Xie, J.; Gong, Q., Ultrafast All-Optical Switching. *Advanced Optical Materials* **2017,** *5* (7).

86. Sounas, D. L.; Alù, A., Non-reciprocal photonics based on time modulation. *Nature Photonics* **2017,** *11* (12), 774-783.

87. Hansteen, F.; Kimel, A.; Kirilyuk, A.; Rasing, T., Nonthermal ultrafast optical control of the magnetization in garnet films. *Physical Review B* **2006,** *73* (1).

88. Singh, N. D.; Moocarme, M.; Edelstein, B.; Punnoose, N.; Vuong, L. T., Anomalously-large photo-induced magnetic response of metallic nanocolloids in aqueous solution using a solar simulator. *Opt. Express* **2012,** *20* (17), 19214-19225.

89. Svirko, Y. P.; Zheludev, N. I., Coherent and incoherent pump–probe specular inverse Faraday effect in media with instantaneous nonlinearity. *Journal of the Optical Society of America B* **1994,** *11* (8), 1388-1393.

90. Zheludev, N. I.; Bennett, P. J.; Loh, H.; Popov, S. V.; Shatwell, I. R.; Svirko, Y. P.; Gusev, V. E.; Kamalov, V. F.; Slobodchikov, E. V., Cubic optical nonlinearity of free electrons in bulk gold. *Opt. Lett.* **1995,** *20* (12), 1368-1370.

91. Wysin, G. M.; Chikan, V.; Young, N.; Dani, R. K., Effects of interband transitions on Faraday rotation in metallic nanoparticles. *J Phys Condens Matter* **2013,** *25* (32), 325302.

92. Beaurepaire, E.; Merle, J.; Daunois, A.; Bigot, J., Ultrafast spin dynamics in ferromagnetic nickel. *Phys Rev Lett* **1996,** *76* (22), 4250-4253.

93. Chen, T.-Y.; Hsia, C.-H.; Chen, H.-Y.; Son, D. H., Size Effect on Chemical Tuning of Spin−Lattice Relaxation Dynamics in Superparamagnetic Nanocrystals. *The Journal of Physical Chemistry C* **2010,** *114* (21), 9713-9719.

94. Yuan, S. h.; Shu, X. Z., A new Faraday rotation glass with a large Verdet constant. *Journal of Applied Physics* **1994,** *75* (10), 6375-6377.

95. Svirko, Y. P.; Zheludev, N. I., *Polarization of Light in Nonlinear Optics*. Wiley: New York, 1998.

96. Wilks, R.; Hughes, N. D.; Hicken, R. J., Investigation of transient linear and circular birefringence in metallic thin films. *Journal of Physics: Condensed Matter* **2003,** *15* (29), 5129.

97. Kruglyak, V. V.; Hicken, R. J.; Ali, M.; Hickey, B. J.; Pym, A. T. G.; Tanner, B. K., Ultrafast third-order optical nonlinearity of noble and transition metal thin films. *Journal of Optics A: Pure and Applied Optics* **2005,** *7* (2), S235-S240.

98. Kruglyak, V. V.; Hicken, R. J.; Ali, M.; Hickey, B. J.; Pym, A. T. G.; Tanner, B. K., Measurement of hot electron momentum relaxation times in metals by femtosecond ellipsometry. *Physical Review B* **2005,** *71* (23).

99. Hsia, C.-H.; Chen, T.-Y.; Son, D. H., Size-Dependent Ultrafast Magnetization Dynamics in Iron Oxide (Fe3O4) Nanocrystals. *Nano Letters* **2008,** *8* (2), 571-576.

100. Kimel, A. V.; Kirilyuk, A.; Usachev, P. A.; Pisarev, R. V.; Balbashov, A. M.; Rasing, T., Ultrafast non-thermal control of magnetization by instantaneous photomagnetic pulses. *Nature* **2005,** *435* (7042), 655-7.

101. Mangin, S.; Gottwald, M.; Lambert, C. H.; Steil, D.; Uhlir, V.; Pang, L.; Hehn, M.; Alebrand, S.; Cinchetti, M.; Malinowski, G.; Fainman, Y.; Aeschlimann, M.; Fullerton, E. E., Engineered materials for all-optical helicity-dependent magnetic switching. *Nat Mater* **2014,** *13* (3), 286-92.

102. Kimel, A. V.; Kirilyuk, A.; Rasing, T., Femtosecond opto-magnetism: ultrafast laser manipulation of magnetic materials. *Laser & Photonics Review* **2007,** *1* (3), 275-287.

103. Wang, C.; Liu, Y., Ultrafast optical manipulation of magnetic order in ferromagnetic materials. *Nano Converg* **2020,** *7* (1), 35.

104. Shafiei, F.; Monticone, F.; Le, K. Q.; Liu, X. X.; Hartsfield, T.; Alu, A.; Li, X., A subwavelength plasmonic metamolecule exhibiting magnetic-based optical Fano resonance. *Nat Nanotechnol* **2013,** *8* (2), 95-9.

105. Moocarme, M.; Dominguez-Juarez, J. L.; Vuong, L. T., Ultralow-intensity magneto-optical and mechanical effects in metal nanocolloids. *Nano Lett* **2014,** *14* (3), 1178-83.

106. Jiang, N.; Zhuo, X.; Wang, J., Active Plasmonics: Principles, Structures, and Applications. *Chemical Reviews* **2018,** *118* (6), 3054-3099.

107. Bonfiglioli, G.; Coen, E.; Malvano, R., Modulation of Conductivity by Surface Charges in Metals. *Physical Review* **1956,** *101* (4), 1281-1284.

108. Elezzabi, A. Y.; Maraghechi, P.; Greig, S. R., Terahertz Plasmonic Field-Induced Conductivity Modulation in Gold. *Sci Rep* **2015,** *5*, 10812.

109. Hogan, N.; Wu, S.; Sheldon, M., Photothermalization and Hot Electron Dynamics in the Steady State. *The Journal of Physical Chemistry C* **2019,** *124* (9), 4931-4945.

110. Hart, T. R.; Aggarwal, R. L.; Lax, B., Temperature Dependence of Raman Scattering in Silicon. *Physical Review B* **1970,** *1* (2), 638-642.

111. Huang, J.; Wang, W.; Murphy, C. J.; Cahill, D. G., Resonant secondary light emission from plasmonic Au nanostructures at high electron temperatures created by pulsed-laser excitation. *Proceedings of the National Academy of Sciences* **2014,** *111* (3), 906.

112. Xie, X.; Cahill, D. G., Thermometry of plasmonic nanostructures by anti-Stokes electronic Raman scattering. *Applied Physics Letters* **2016,** *109* (18), 183104.

113. Carattino, A.; Caldarola, M.; Orrit, M., Gold Nanoparticles as Absolute Nanothermometers. *Nano Letters* **2018,** *18* (2), 874-880.

114. Hogan, N.; Sheldon, M., Comparing steady state photothermalization dynamics in copper and gold nanostructures. *The Journal of Chemical Physics* **2020,** *152* (6), 061101.

115. Hogan, N.; Wu, S.; Sheldon, M., Photothermalization and Hot Electron Dynamics in the Steady State. *The Journal of Physical Chemistry C* **2020,** *124* (9), 4931-4945.

116. Wu, S.; Hsu-Cheng Cheng, O.; Zhao, B.; Hogan, N.; Lee, A.; Son, D. H.; Sheldon, M. The Connection Between Plasmon Decay Dynamics and the SERS background: Inelastic Scattering from Non-Thermal and Hot Carriers 2020, p. arXiv:2010.06839. https://ui.adsabs.harvard.edu/abs/2020arXiv201006839W (accessed October 01, 2020).

117. Otto, A.; Akemann, W.; Pucci, A., Normal Bands in Surface-Enhanced Raman Scattering (SERS) and Their Relation to the Electron-Hole Pair Excitation Background in SERS. *Israel Journal of Chemistry* **2006,** *46* (3), 307-315.

118. Yan, F.; Demir, H. V., LEDs using halide perovskite nanocrystal emitters. *Nanoscale* **2019,** *11* (24), 11402-11412.

119. Stylianakis, M. M.; Maksudov, T.; Panagiotopoulos, A.; Kakavelakis, G.; Petridis, K., Inorganic and Hybrid Perovskite Based Laser Devices: A Review. *Materials* **2019,** *12* (6).

120. Zhang, X.; Sun, C.; Zhang, Y.; Wu, H.; Ji, C.; Chuai, Y.; Wang, P.; Wen, S.; Zhang, C.; Yu, W. W., Bright Perovskite Nanocrystal Films for Efficient Light-Emitting Devices. *Journal of Physical Chemistry Letters* **2016,** *7* (22), 4602-4610.

121. Zhang, L.; Yang, X.; Jiang, Q.; Wang, P.; Yin, Z.; Zhang, X.; Tan, H.; Yang, Y. M.; Wei, M.; Sutherland, B. R.; Sargent, E. H.; You, J., Ultra-bright and highly efficient inorganic based perovskite light-emitting diodes. *Nature Communications* **2017,** *8*, 15640.

122. Deng, W.; Xu, X.; Zhang, X.; Zhang, Y.; Jin, X.; Wang, L.; Lee, S.-T.; Jie, J., Organometal Halide Perovskite Quantum Dot Light-Emitting Diodes. *Advanced Functional Materials* **2016,** *26* (26), 4797-4802.

123. Dutta, A.; Behera, R. K.; Pal, P.; Baitalik, S.; Pradhan, N., Near-Unity Photoluminescence Quantum Efficiency for All $CsPbX_3$ (X=Cl, Br, and I) Perovskite Nanocrystals: A Generic Synthesis Approach. *Angewandte Chemie, International Edition in English* **2019,** *58* (17), 5552-5556.

124. Di Stasio, F.; Christodoulou, S.; Huo, N.; Konstantatos, G., Near-Unity Photoluminescence Quantum Yield in $CsPbBr_3$ Nanocrystal Solid-State Films via Postsynthesis Treatment with Lead Bromide. *Chemistry of Materials* **2017,** *29* (18), 7663-7667.

125. Roman, B. J.; Sheldon, M., The role of mid-gap states in all-inorganic $CsPbBr_3$ nanoparticle one photon up-conversion. *Chemical Communications* **2018,** *54* (50), 6851-6854.

126. Rodríguez Ortiz, F. A.; Roman, B. J.; Wen, J.-R.; Mireles Villegas, N.; Dacres, D. F.; Sheldon, M. T., The role of gold oxidation state in the synthesis of Au-$CsPbX_3$ heterostructure or lead-free $Cs_2Au^{I}Au^{III}X_6$ perovskite nanoparticles. *Nanoscale* **2019,** *11* (39), 18109-18115.

127. Nedelcu, G.; Protesescu, L.; Yakunin, S.; Bodnarchuk, M. I.; Grotevent, M. J.; Kovalenko, M. V., Fast Anion-Exchange in Highly Luminescent Nanocrystals of Cesium Lead Halide Perovskites ($CsPbX_3$, X = Cl, Br, I). *Nano Letters* **2015,** *15* (8), 5635-5640.

128. Parobek, D.; Dong, Y.; Qiao, T.; Rossi, D.; Son, D. H., Photoinduced Anion Exchange in Cesium Lead Halide Perovskite Nanocrystals. *Journal of the American Chemical Society* **2017,** *139* (12), 4358-4361.

129. Sadhanala, A.; Ahmad, S.; Zhao, B.; Giesbrecht, N.; Pearce, P. M.; Deschler, F.; Hoye, R. L.; Godel, K. C.; Bein, T.; Docampo, P.; Dutton, S. E.; De Volder, M. F.; Friend, R. H., Blue-Green Color Tunable Solution Processable Organolead Chloride-Bromide Mixed Halide Perovskites for Optoelectronic Applications. *Nano Lett* **2015,** *15* (9), 6095-101.

130. Miao, Y.; Ke, Y.; Wang, N.; Zou, W.; Xu, M.; Cao, Y.; Sun, Y.; Yang, R.; Wang, Y.; Tong, Y.; Xu, W.; Zhang, L.; Li, R.; Li, J.; He, H.; Jin, Y.; Gao, F.; Huang, W.; Wang, J., Stable and bright formamidinium-based perovskite light-emitting diodes with high energy conversion efficiency. *Nature Communications* **2019,** *10* (1).

131. Chiba, T.; Hayashi, Y.; Ebe, H.; Hoshi, K.; Sato, J.; Sato, S.; Pu, Y.-J.; Ohisa, S.; Kido, J., Anion-exchange red perovskite quantum dots with ammonium iodine salts for highly efficient light-emitting devices. *Nature Photonics* **2018,** *12* (11), 681-687.

132. Huang, H.; Bodnarchuk, M. I.; Kershaw, S. V.; Kovalenko, M. V.; Rogach, A. L., Lead Halide Perovskite Nanocrystals in the Research Spotlight: Stability and Defect Tolerance. *ACS Energy Letters* **2017,** *2* (9), 2071-2083.

133. Kim, Y.-H.; Wolf, C.; Kim, Y.-T.; Cho, H.; Kwon, W.; Do, S.; Sadhanala, A.; Park, C. G.; Rhee, S.-W.; Im, S. H.; Friend, R. H.; Lee, T.-W., Highly Efficient Light-Emitting Diodes of Colloidal Metal–Halide Perovskite Nanocrystals beyond Quantum Size. *ACS Nano* **2017,** *11* (7), 6586-6593.

134. Dohner, E. R.; Jaffe, A.; Bradshaw, L. R.; Karunadasa, H. I., Intrinsic white-light emission from layered hybrid perovskites. *J Am Chem Soc* **2014,** *136* (38), 13154-7.

135. Mao, J.; Lin, H.; Ye, F.; Qin, M.; Burkhartsmeyer, J. M.; Zhang, H.; Lu, X.; Wong, K. S.; Choy, W. C. H., All-Perovskite Emission Architecture for White Light-Emitting Diodes. *ACS Nano* **2018,** *12* (10), 10486-10492.

136. Guhrenz, C.; Benad, A.; Ziegler, C.; Haubold, D.; Gaponik, N.; Eychmüller, A., Solid-State Anion Exchange Reactions for Color Tuning of $CsPbX_3$ Perovskite Nanocrystals. *Chemistry of Materials* **2016,** *28* (24), 9033-9040.

137. Su, Y.; Chen, X.; Ji, W.; Zeng, Q.; Ren, Z.; Su, Z.; Liu, L., Highly Controllable and Efficient Synthesis of Mixed-Halide $CsPbX_3$ (X = Cl, Br, I) Perovskite QDs toward the Tunability of Entire Visible Light. *ACS Applied Materials & Interfaces* **2017,** *9* (38), 33020-33028.

138. Zhang, H.; Fu, X.; Tang, Y.; Wang, H.; Zhang, C.; Yu, W. W.; Wang, X.; Zhang, Y.; Xiao, M., Phase segregation due to ion migration in all-inorganic mixed-halide perovskite nanocrystals. *Nature Communications* **2019,** *10* (1), 1088.

139. Slotcavage, D. J.; Karunadasa, H. I.; McGehee, M. D., Light-Induced Phase Segregation in Halide-Perovskite Absorbers. *ACS Energy Letters* **2016,** *1* (6), 1199-1205.

140. Vashishtha, P.; Halpert, J. E., Field-Driven Ion Migration and Color Instability in Red-Emitting Mixed Halide Perovskite Nanocrystal Light-Emitting Diodes. *Chemistry of Materials* **2017,** *29* (14), 5965-5973.

141. Gratia, P.; Grancini, G.; Audinot, J.-N.; Jeanbourquin, X.; Mosconi, E.; Zimmermann, I.; Dowsett, D.; Lee, Y.; Grätzel, M.; De Angelis, F.; Sivula, K.; Wirtz, T.; Nazeeruddin, M. K., Intrinsic Halide Segregation at Nanometer Scale Determines the High Efficiency of Mixed Cation/Mixed Halide Perovskite Solar Cells. *Journal of the American Chemical Society* **2016,** *138* (49), 15821-15824.

142. Brennan, M. C.; Draguta, S.; Kamat, P. V.; Kuno, M., Light-Induced Anion Phase Segregation in Mixed Halide Perovskites. *ACS Energy Letters* **2018,** *3* (1), 204-213.

143. Dong, Y.; Qiao, T.; Kim, D.; Parobek, D.; Rossi, D.; Son, D. H., Precise Control of Quantum Confinement in Cesium Lead Halide Perovskite Quantum Dots via Thermodynamic Equilibrium. *Nano Lett.* **2018,** *18* (6), 3716-3722.

144. Dong, Y.; Qiao, T.; Kim, D.; Rossi, D.; Ahn, S. J.; Son, D. H., Controlling Anisotropy of Quantum-Confined $CsPbBr_3$ Nanocrystals by Combined Use of Equilibrium and Kinetic Anisotropy. *Chemistry of Materials* **2019,** *31* (15), 5655-5662.

145. Li, Q.; Yang, Y.; Que, W.; Lian, T., Size- and Morphology-Dependent Auger Recombination in $CsPbBr_3$ Perovskite Two-Dimensional Nanoplatelets and One-Dimensional Nanorods. *Nano Letters* **2019,** *19* (8), 5620-5627.

146. Weidman, M. C.; Goodman, A. J.; Tisdale, W. A., Colloidal Halide Perovskite Nanoplatelets: An Exciting New Class of Semiconductor Nanomaterials. *Chemistry of Materials* **2017,** *29* (12), 5019-5030.

147. Liang, Z.; Zhao, S.; Xu, Z.; Qiao, B.; Song, P.; Gao, D.; Xu, X., Shape-Controlled Synthesis of All-Inorganic $CsPbBr_3$ Perovskite Nanocrystals with Bright Blue Emission. *ACS Applied Materials & Interfaces* **2016,** *8* (42), 28824-28830.

148. Olkhovets, A.; Hsu, R. C.; Lipovskii, A.; Wise, F. W., Size-Dependent Temperature Variation of the Energy Gap in Lead-Salt Quantum Dots. *Physical Review Letters* **1998,** *81* (16), 3539-3542.

149. Sagar, D. M.; Cooney, R. R.; Sewall, S. L.; Dias, E. A.; Barsan, M. M.; Butler, I. S.; Kambhampati, P., Size dependent, state-resolved studies of exciton-phonon couplings in strongly confined semiconductor quantum dots. *Physical Review B* **2008,** *77* (23).

150. Nomura, S.; Kobayashi, T., Exciton—LO-phonon couplings in spherical semiconductor microcrystallites. *Physical Review B* **1992,** *45* (3), 1305-1316.

151. Morello, G.; De Giorgi, M.; Kudera, S.; Manna, L.; Cingolani, R.; Anni, M., Temperature and Size Dependence of Nonradiative Relaxation and Exciton−Phonon Coupling in Colloidal CdTe Quantum Dots. *The Journal of Physical Chemistry C* **2007,** *111* (16), 5846-5849.

152. Mack, T. G.; Jethi, L.; Kambhampati, P., Temperature Dependence of Emission Line Widths from Semiconductor Nanocrystals Reveals Vibronic Contributions to Line Broadening Processes. *Journal of Physical Chemistry C* **2017,** *121* (51), 28537-28545.

153. Yazdani, N.; Bozyigit, D.; Vuttivorakulchai, K.; Luisier, M.; Infante, I.; Wood, V., Tuning Electron-Phonon Interactions in Nanocrystals through Surface Termination. *Nano Lett* **2018,** *18* (4), 2233-2242.

154. Schnitzenbaumer, K. J.; Dukovic, G., Comparison of Phonon Damping Behavior in Quantum Dots Capped with Organic and Inorganic Ligands. *Nano Lett* **2018,** *18* (6), 3667-3674.

155. Diroll, B. T.; Zhou, H.; Schaller, R. D., Low-Temperature Absorption, Photoluminescence, and Lifetime of $CsPbX_3$ (X = Cl, Br, I) Nanocrystals. *Advanced Functional Materials* **2018,** *28* (30).

156. Ai, B.; Liu, C.; Deng, Z.; Wang, J.; Han, J.; Zhao, X., Low temperature photoluminescence properties of $CsPbBr_3$ quantum dots embedded in glasses. *Physical Chemistry Chemical Physics* **2017,** *19* (26), 17349-17355.

157. Li, J.; Yuan, X.; Jing, P.; Li, J.; Wei, M.; Hua, J.; Zhao, J.; Tian, L., Temperature-dependent photoluminescence of inorganic perovskite nanocrystal films. *RSC Advances* **2016,** *6* (82), 78311-78316.

158. Wei, K.; Xu, Z.; Chen, R.; Zheng, X.; Cheng, X.; Jiang, T., Temperature-dependent excitonic photoluminescence excited by two-photon absorption in perovskite $CsPbBr_3$ quantum dots. *Opt. Lett.* **2016,** *41* (16), 3821-4.

159. Protesescu, L.; Yakunin, S.; Bodnarchuk, M. I.; Krieg, F.; Caputo, R.; Hendon, C. H.; Yang, R. X.; Walsh, A.; Kovalenko, M. V., Nanocrystals of Cesium Lead Halide Perovskites ($CsPbX_3$, X = Cl, Br, and I): Novel Optoelectronic Materials Showing Bright Emission with Wide Color Gamut. *Nano Lett.* **2015,** *15* (6), 3692-6.

160. Mooney, J.; Kambhampati, P., Get the Basics Right: Jacobian Conversion of Wavelength and Energy Scales for Quantitative Analysis of Emission Spectra. *Journal of Physical Chemistry Letters* **2013,** *4* (19), 3316-3318.

161. Chen, H.-Y.; Maiti, S.; Nelson, C. A.; Zhu, X.; Son, D. H., Tuning Temperature Dependence of Dopant Luminescence via Local Lattice Strain in Core/Shell Nanocrystal Structure. *The Journal of Physical Chemistry C* **2012,** *116* (44), 23838-23843.

162. Lao, X.; Zhou, W.; Bao, Y.; Wang, X.; Yang, Z.; Wang, M.; Xu, S., Photoluminescence signatures of thermal expansion, electron-phonon coupling and phase transitions in cesium lead bromide perovskite nanosheets. *Nanoscale* **2020**.

163. Kim, D.; Yokota, H.; Shimura, K.; Nakayama, M., Temperature dependence of photoluminescence dynamics of self-assembled monolayers of CdSe quantum dots: the influence of the bound-exciton state. *Physical Chemistry Chemical Physics* **2013,** *15* (48), 21051-7.

164. Vossmeyer, T.; Katsikas, L.; Giersig, M.; Popovic, I. G.; Diesner, K.; Chemseddine, A.; Eychmueller, A.; Weller, H., CdS Nanoclusters: Synthesis, Characterization, Size Dependent Oscillator Strength, Temperature Shift of the Excitonic

Transition Energy, and Reversible Absorbance Shift. *The Journal of Physical Chemistry* **1994,** *98* (31), 7665-7673.

165. Saran, R.; Heuer-Jungemann, A.; Kanaras, A. G.; Curry, R. J., Giant Bandgap Renormalization and Exciton–Phonon Scattering in Perovskite Nanocrystals. *Advanced Optical Materials* **2017,** *5* (17), 1700231.

166. Yu, C.; Chen, Z.; J. Wang, J.; Pfenninger, W.; Vockic, N.; Kenney, J. T.; Shum, K., Temperature dependence of the band gap of perovskite semiconductor compound CsSnI3. *Journal of Applied Physics* **2011,** *110* (6).

167. Ramade, J.; Andriambariarijaona, L. M.; Steinmetz, V.; Goubet, N.; Legrand, L.; Barisien, T.; Bernardot, F.; Testelin, C.; Lhuillier, E.; Bramati, A.; Chamarro, M., Exciton-phonon coupling in a $CsPbBr_3$ single nanocrystal. *Applied Physics Letters* **2018,** *112* (7).

168. Wright, A. D.; Verdi, C.; Milot, R. L.; Eperon, G. E.; Perez-Osorio, M. A.; Snaith, H. J.; Giustino, F.; Johnston, M. B.; Herz, L. M., Electron-phonon coupling in hybrid lead halide perovskites. *Nature Communications* **2016,** *7*.

169. Rudin, S.; Reinecke, T. L.; Segall, B., Temperature-dependent exciton linewidths in semiconductors. *Physical Review B* **1990,** *42* (17), 11218-11231.

170. Tang, F.; Su, Z.; Ye, H.; Zhu, Y.; Dai, J.; Xu, S., Anomalous variable-temperature photoluminescence of $CsPbBr_3$ perovskite quantum dots embedded into an organic solid. *Nanoscale* **2019,** *11* (43), 20942-20948.

171. Stoumpos, C. C.; Malliakas, C. D.; Peters, J. A.; Liu, Z.; Sebastian, M.; Im, J.; Chasapis, T. C.; Wibowo, A. C.; Chung, D. Y.; Freeman, A. J.; Wessels, B. W.; Kanatzidis, M. G., Crystal Growth of the Perovskite Semiconductor $CsPbBr_3$: A New Material for High-Energy Radiation Detection. *Crystal Growth & Design* **2013,** *13* (7), 2722-2727.

172. Lin, C.; Gong, K.; Kelley, D. F.; Kelley, A. M., Size-Dependent Exciton–Phonon Coupling in CdSe Nanocrystals through Resonance Raman Excitation Profile Analysis. *The Journal of Physical Chemistry C* **2015,** *119* (13), 7491-7498.

173. Kelley, A. M., Exciton-optical phonon coupling in II-VI semiconductor nanocrystals. *Journal of Chemical Physics* **2019,** *151* (14), 140901.

174. Isarov, M.; Grumbach, N.; Maikov, G. I.; Tilchin, J.; Jang, Y.; Sashchiuk, A.; Lifshitz, E., The effect of low temperature coating and annealing on structural and optical properties of CdSe/CdS core/shell QDs. *Lithuanian Journal of Physics* **2016,** *55* (4).

175. Miyata, K.; Meggiolaro, D.; Trinh, M. T.; Joshi, P. P.; Mosconi, E.; Jones, S. C.; De Angelis, F.; Zhu, X. Y., Large polarons in lead halide perovskites. *Science Advances* **2017,** *3* (8).

176. Zhu, X. Y.; Podzorov, V., Charge Carriers in Hybrid Organic-Inorganic Lead Halide Perovskites Might Be Protected as Large Polarons. *J. Phys. Chem. Lett.* **2015,** *6* (23), 4758-61.

177. Frost, J. M., Calculating polaron mobility in halide perovskites. *Physical Review B* **2017,** *96* (19).

178. Rossi, D.; Wang, H.; Dong, Y.; Qiao, T.; Qian, X.; Son, D. H., Light-Induced Activation of Forbidden Exciton Transition in Strongly Confined Perovskite Quantum Dots. *ACS Nano* **2018,** *12* (12), 12436-12443.

179. Jin, H.; Ahn, M.; Jeong, S.; Han, J. H.; Yoo, D.; Son, D. H.; Cheon, J., Colloidal Single-Layer Quantum Dots with Lateral Confinement Effects on 2D Exciton. *Journal of the American Chemical Society* **2016,** *138* (40), 13253-13259.

180. Jin, H.; Baek, B.; Kim, D.; Wu, F.; Batteas, J. D.; Cheon, J.; Son, D. H., Effects of Direct Solvent-Quantum Dot Interaction on the Optical Properties of Colloidal Monolayer WS_2 Quantum Dots. *Nano Letters* **2017,** *17* (12), 7471-7477.

181. Battiato, M.; Barbalinardo, G.; Oppeneer, P. M., Quantum theory of the inverse Faraday effect. *Physical Review B* **2014,** *89* (1).

182. Alekhin, A.; Razdolski, I.; Berritta, M.; Bürstel, D.; Temnov, V.; Diesing, D.; Bovensiepen, U.; Woltersdorf, G.; Oppeneer, P. M.; Melnikov, A., Magneto-optical properties of Au upon the injection of hot spin-polarized electrons across Fe/Au(0 0 1) interfaces. *Journal of Physics: Condensed Matter* **2019,** *31* (12).

183. Boyd, R. W.; Shi, Z.; De Leon, I., The third-order nonlinear optical susceptibility of gold. *Optics Communications* **2014,** *326*, 74-79.

184. Hache, F.; Ricard, D.; Flytzanis, C.; Kreibig, U., The optical kerr effect in small metal particles and metal colloids: The case of gold. *Applied Physics A* **1988,** *47* (4), 347-357.

APPENDIX A

SUPPLEMENTAL INFORMATION OF CHAPTER II

A.1 Verdet constant of Faraday effect and the IFE in absorbing medium

The IFE expression in Eq. 1.4 does not account for the effect of dissipation and resonance in an absorbing medium. However, if these contributions are large, they will cause a difference in the value of the Verdet constant of the Faraday effect and the IFE. We consider the damping constant and resonance condition under a classical treatment.[181] The complex Verdet constant for gold colloid can be written as:

$$\upsilon_{FE} \approx -\frac{\pi N e^3}{m_e^2 \lambda_v n} \frac{\omega}{\left(\omega_0^2 + i\gamma\omega - \omega^2\right)^2} = -6.48 \times 10^{-9} + 1.51 \times 10^{-8}\, i \quad \text{(B.1)}$$

where N is electron density of gold, $N = 5.57 \times 10^{28}\ m^{-3}$, e is electron charge, $e = 1.602 \times 10^{-19}$ c, m_e is effective mass of gold, $m_e = 9.02 \times 10^{31}$ kg, λ_v is the wavelength of the light in vacuum, $\lambda_v = 5.15 \times 10^{-7}$ m, n is the refractive index of the gold at 515 nm, $n = 0.71912 + 2.0225i$, ω is the angular frequency of the incident light, $\omega = 3.66 \times 10^{15}$ rad/s, γ is the bulk damping constant of gold, $\gamma = 1.26 \times 10^{14}$ Hz and ω_0 is 0, in the limit that the Au is approximated as a Drude metal. Then, the Verdet constant of the IFE can be written as

$$\upsilon_{IFE} = -\frac{\pi N e^3}{m_e^2 \lambda_v n_0} \frac{\omega}{\left(\omega^2 - \omega_0^2\right)^2 + \gamma^2 \omega^2} = -5.42 \times 10^{-9} + 1.55 \times 10^{-8} i \qquad \text{(B.2)}$$

The difference between υ_{FE} and υ_{IFE} is 16%. While small, this difference is accounted for in all calculations throughout the study.

A.2 Calculation of the induced magnetization during the IFE experiment

In a Faraday rotation experiment, the applied magnetic field is related to the magnetization of the AuNP colloid by the following expression:

$$\vec{B}_{app} = \mu_0(\vec{H}+\vec{M}) = \mu_0\left(\frac{\vec{M}}{\chi_v}+\vec{M}\right) = \mu_0\left(\frac{1}{\chi_v}+1\right)\vec{M} \qquad (B.3)$$

where μ_0 is permeability of vacuum, μ_0 = 1.25664 x 10^{-6} and χ_v is volume magnetic susceptibility of Au, $\chi_v = -3.44 \times 10^{-5}$. Therefore Eq. 2.3 in the main text can be written as:

$$\Delta\theta = \upsilon\vec{B}_{app}L = \upsilon_{FE}\mu_0\left(\frac{1}{\chi_v}+1\right)\vec{M}_{ind}L \qquad (B.4)$$

The measured magnetization of the AuNP colloid in the Faraday rotation experiment was -9.58 A/m. By accounting for the 16% difference between υ_{FE} and υ_{IFE} in this study, we can obtain the induced magnetization during the IFE experiment by measuring the induced rotation $\Delta\theta$.

However, the attenuation of the pump intensity is not negligible, so the induced magnetization decreases along the optical path in the colloid. Based on Eq. 1.4 in the main text, the induced magnetization is linear with the pump intensity, so the measured overall Faraday rotation will be determined by the average pump intensity along the beam path, as shown below.

Based on the extinction coefficient $\varepsilon = 8.89 \times 10^{10}$ $M^{-1}cm^{-1}$ at the excitation wavelength 515 nm, the AuNP concentration was 6.37×10^{-12} M. The excitation intensity, I, as a function of position, x, can be written as:

$$I(x) = I_0 10^{-A} = I_0 10^{-\varepsilon c x} \qquad (B.5)$$

Since the effective magnetic field is linear with excitation intensity, we can write

$$\overrightarrow{M}_{ind}(x) = \overrightarrow{M}^{0}_{ind} 10^{-\varepsilon c x} \quad \text{(B.6)}$$

Then the induced rotation $\Delta\theta$ can be written as:

$$\Delta\theta = \int_0^{0.2} \upsilon_{IFE}\mu_0 \left(\frac{1}{\chi_v}+1\right) \overrightarrow{M}_{ind}(x)dx$$

$$= \upsilon_{IFE}\mu_0 \left(\frac{1}{\chi_v}+1\right) \int_0^{0.2} \overrightarrow{M}^{0}_{ind} 10^{-\varepsilon c x}\, dx$$

$$= 0.176\, \upsilon_{IFE}\mu_0 \left(\frac{1}{\chi_v}+1\right) \overrightarrow{M}^{0}_{ind} \quad \text{(B.7)}$$

With 9.1×10^{13} W/m^2 excitation intensity, and the induced rotation $\Delta\theta = 0.1587^{o}$, therefore $\overrightarrow{M}^{0}_{ind}$ = -1.04 A/m. This light-induced magnetization can be thought of equivalently in terms of what applied external magnetic field, $\overrightarrow{B}_{eff}$ in the main text, would result in the same magnetization, as commonly discussed in several other reports of the IFE.[36, 100] Here, the maximum measured $\overrightarrow{B}_{eff}$ = 0.038T.

A.3 Calculation of magnetic moment per gold atom

With $\overrightarrow{M}_{ind}$ measured in the IFE experiment, the magnetic moment per gold nanoparticle m_{AuNP} and magnetic moment per gold atom m_{Au} can be calculated by

$$\overrightarrow{M}_{ind} = \frac{N_{AuNP} \cdot m_{AuNP}}{V} = \frac{N_{AuNP} \cdot N_{atom} \cdot m_{Au}}{V} \quad \text{(B.8)}$$

where N_{AuNP} is number of Au nanoparticles within the pump beam volume V, and N_{atom} is the number of Au atoms per nanoparticle, $N_{atom} = 3.1 \times 10^7$ for a 100nm diameter AuNP.

A.4 Comparison of induced magnetic moment with other literature

The induced magnetic moment in Au films and AuNPs is compared, and the enhancement factor in the AuNPs is estimated. The Au film data is based on previous reports of pump-probe experiments on Au films. The calculations here for m_{Au} are the same as in section A.2 and A.3 above.

	Photon energy (eV)	Path length (cm)	Induced rotation (deg)	Intensity ($\times 10^{13}$ W/m^2)	[b,c] $\overrightarrow{M}_{ind}$(A/m)	m_{Au} (μ_B)
V. V. Kruglyak *et al.*[98]	1.55	[a] 1.3×10^{-6}	1×10^{-3}	12.6	-153.5	-2.80×10^{-4}
V. V. Kruglyak *et al.*[97]	1.55	[a] 1.3×10^{-6}	2.5×10^{-3}	12.6	-383.7	-7.01×10^{-4}
[d] A. Alekhin *et al.*[182]						$\sim 1 \times 10^{-3}$
This study	2.41	0.2	1.59×10^{-2}	9.09	-1.04	-9.49×10^{-1}

[a] The path length in a gold film is estimated by the skin depth = (1/absorption coefficient).
[b] The Verdet constant of gold film is extracted from the report by J. McGroddy *et al.*,[23] and by accounting for the difference between υ_{FE} and υ_{IFE}.
[c] The induced magnetization is normalized to the same excitation intensity and excitation frequency, as shown in Hertel's expression.[41]
[d] The induced magnetic moment in an Au film is generated by the injection of ultrafast spin-polarized electrons from a fs-laser-excited iron thin film.

A.5 Origin of the enhanced magnetism in AuNP

Based on Eq. 1.4 observation of enhanced magnetization could result from either enhanced local optical field, an increase of the Verdet constant, or both. In AuNPs, the maximum local optical field enhancement is estimated to be ~5×, and this is insufficient to explain the ~1000× enhancement observed in our experiment.[43] Therefore, our data implies that the rest of the enhancement is due to the change in the Verdet constant. In our static Faraday rotation experiment, we observed that the Verdet constant of AuNPs is ~16× larger than bulk Au films. Even considering the plasmonic optical field concentration and

the enhanced Verdet constant measured experimentally, still we observe another factor of 10 larger induced magnetism compared with bulk Au.

We can also understand the enhanced magnetization through the third-order susceptibility $\chi^{(3)}$. Based on Eq. 1.3 and 1.4,

$$\Delta\theta = \upsilon\vec{B}_{app}L \propto \upsilon\cdot\vec{M}_{ind}\cdot L \propto \upsilon\cdot\upsilon\cdot I\cdot L \quad (B.9)$$

And from Eq. 2.1 and 2.2

$$\Delta\theta \propto \chi^{(3)}\cdot L\cdot I \quad (B.10)$$

By comparing these two expressions, we can conclude that if the Verdet constant is enhanced, $\chi^{(3)}$ must be enhanced as well. In this study, the $\chi^{(3)}$ can be estimated under the following assumptions: First, the local optical field enhancement at AuNP surface is ~5×. Second, $\chi^{(3)} \approx \chi^{(3)}_{xxyy} - \chi^{(3)}_{xyyx}$, since $\chi^{(3)}_{xyyx}$ is usually 1 order of magnitude smaller than $\chi^{(3)}_{xxyy}$.[183] Third, $\chi^{(3)}$ of the active medium (AuNP colloid solution) and the third-order susceptibility of Au, $\chi^{(3)}_m$ is related through the local field correction[184]:

$$\chi^{(3)} = pf_l^{\,2}|f_l|^2\chi^{(3)}_m \quad (B.10)$$

Where p is volume fraction of AuNP in the colloid solution, $p = 2\times10^{-6}$, f_l is the local field factor in Maxwell-Garnett approximation, $f_l(\omega) = \frac{3\varepsilon_d}{\varepsilon_m(\omega)+2\varepsilon_d}$, where ε_d is the dielectric constant of surrounding (water) at 515nm, $\varepsilon_d = 1.78$, ε_m is the dielectric constant of Au at 515 nm, $\varepsilon_m = -3.57+2.91i$. Under our experimental condition (2 mm path length, 9.1×10^9 W/cm^2 excitation intensity), we estimate $\chi^{(3)} = 9.5 \times 10^{-9}$ esu, which is ~10× compared to the reported value of bulk Au films.[183] Thus, this analysis of the Verdet constant and $\chi^{(3)}$ emphasizes that the enhanced magnetism is not only due to the plasmonic optical field

concentration, but also a result of the fundamental change in the electronic properties that give rise to the differing dielectric function of the AuNPs compared with bulk Au.

APPENDIX B

SUPPLEMENTAL INFORMATION OF CHAPTER IV

B.1 Spectral line shape analysis

The raw PL spectra, I(λ), expressed in count/nm vs wavelength (nm), is converted into the spectra on energy axis, I(E), counts/eV vs eV through Jacobian conversion.[160] I(E) is further converted to the spectral line shape, S(E) , which is directly proportional to Frank-Condon factor as shown in Eq. B.1.[161] c, n and M_D are the speed of light, optical dielectric constant, and transition dipole moment, respectively.

$$S(E) = I(E)/E^3 = (32\pi^3/3\hbar^4c^3)n^3|M_D|^2FC(E) \qquad (B.1)$$

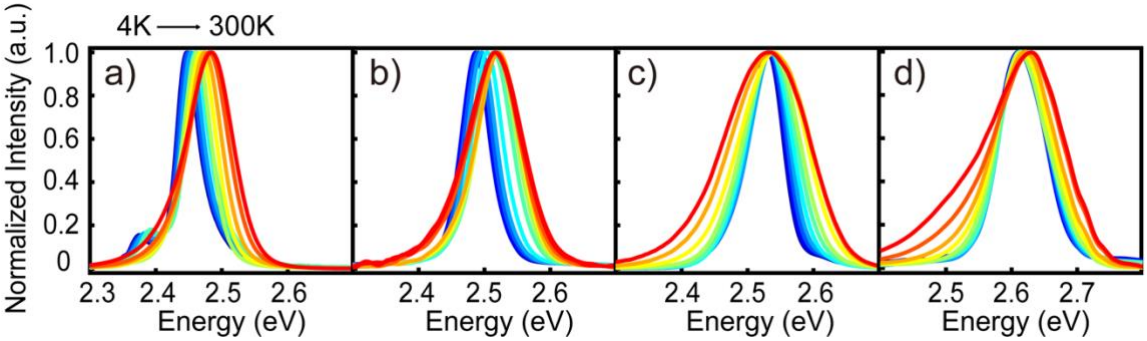

Figure B.1: Normalized spectral line shape, S(E), of (a) 6.3 nm (b) 5.3 nm (c) 4.7 nm (d) 3.9 nm $CsPbBr_3$ QDs samples at temperatures between 4 and 300K.